

This work was written as part of one of the author's official duties as an Employee of the United States Government and is therefore a work of the United States Government. In accordance with 17 U.S.C. 105, no copyright protection is available for such works under U.S. Law.

Public Domain Mark 1.0

<https://creativecommons.org/publicdomain/mark/1.0/>

Access to this work was provided by the University of Maryland, Baltimore County (UMBC) ScholarWorks@UMBC digital repository on the Maryland Shared Open Access (MD-SOAR) platform.

Please provide feedback

Please support the ScholarWorks@UMBC repository by emailing scholarworks-group@umbc.edu and telling us what having access to this work means to you and why it's important to you. Thank you.



The thermal infrared optical depth of mineral dust retrieved from integrated CALIOP and IIR observations

Jianyu Zheng^{a,b}, Zhibo Zhang^{a,b,*}, Anne Garnier^{c,d}, Hongbin Yu^e, Qianqian Song^{a,b},
Chenxi Wang^{b,e}, Philippe Dubuisson^f, Claudia Di Biagio^g

^a Department of Physics, University of Maryland Baltimore County, Baltimore, MD, USA

^b Joint Center for Earth Systems Technology, University of Maryland Baltimore County, Baltimore, MD, USA

^c Science Systems and Applications, Inc., Hampton, Virginia, USA

^d NASA Langley Research Center, Hampton, Virginia, USA

^e NASA Goddard Space Flight Center, Greenbelt, MD, USA

^f Laboratoire d'Optique Atmosphérique, Université de Lille, Lille, France

^g Université de Paris and Univ Paris Est Creteil, CNRS, LISA, F-75013 Paris, France

ARTICLE INFO

Keywords:

Aerosol
Dust
Thermal infrared
Radiative effect
IIR
CALIOP

ABSTRACT

Recent studies have suggested that global climate models tend to underestimate dust particle size in particular, the very coarse mode, leading to an underestimated direct radiative effect (DRE) of dust in the longwave (LW) thermal infrared (TIR) region. However, the magnitude of LW DRE remains highly uncertain, because of limited observations of dust optical depth at the TIR (DAOD_{TIR}). This study presents a simple approach to retrieve the DAOD_{TIR} over the oceans during nighttime through synergistic use of observations from the Infrared Imaging Radiometer (IIR) and the Cloud-Aerosol Lidar with Orthogonal Polarization (CALIOP), both onboard of the Cloud-Aerosol Lidar and Infrared Pathfinder Satellite Observations (CALIPSO) mission. For each cloud-free dust-laden profile identified by the IIR-CALIOP observation, a Lookup-Table (LUT) of the 10.6 μm IIR band brightness temperatures (BT) difference (dBT) under different DAOD_{TIR} with respect to their dust-free BTs is constructed based on the CALIOP retrieved dust vertical profile and a priori dust scattering properties using a fast radiative transfer model. Then the DAOD_{TIR} is retrieved by projecting the IIR-observed dBT on the LUT. Sensitivity studies show that the DAOD_{TIR} retrieval at 10.6 μm is more susceptible to the dust particle size distribution (PSD) assumption than dust refractive indices. To estimate the uncertainty caused by PSD assumption, two DAOD_{TIR} retrieval products, one based on the dust PSD from the AERONET at Cape Verde and the other on an in situ measured PSD from the recent Fennec campaign, are provided. The retrieval uncertainty is mainly contributed by the BT difference between the observation and simulation using auxiliary atmospheric data. The climatology of the retrieval from 2013 to 2019 shows reasonable spatiotemporal variations of DAOD_{TIR} with the global-averaged value of 0.008 and 0.013 based on different pre-assumed dust PSDs. Climatological results agree reasonably well with two independent DAOD_{TIR} retrieval products based on the Infrared Atmospheric Sounding Interferometer (IASI) over the active dust transport regions, such as North and Tropical Atlantic ($r = 0.9$ and $r = 0.8$) and Indian Ocean ($r = 0.8$). The seasonal and interannual variation is also well-compared ($r = 0.76$) with AERONET coarse-mode AOD at 97 selected sites. The synergistic CALIOP observation allows the retrieved DAOD_{TIR} to directly compare with the extrapolated DAOD_{TIR} from DAOD in the visible (i.e., 532 nm), which helps evaluate the observational constraints on DAOD_{TIR}. Our study clearly reveals that the retrieved DAOD_{TIR} from IIR is much less susceptible to various uncertainties than converted results from CALIOP. It also offers a unique prospect of collocated active lidar and passive IR observations for retrieving dust DAOD_{TIR}.

* Corresponding author at: Department of Physics, University of Maryland Baltimore County, Baltimore, MD, USA

E-mail address: zzbatmos@umbc.edu (Z. Zhang).

<https://doi.org/10.1016/j.rse.2021.112841>

Received 30 June 2021; Received in revised form 3 December 2021; Accepted 4 December 2021

Available online 23 December 2021

0034-4257/© 2021 The Authors. Published by Elsevier Inc. This is an open access article under the CC BY license (<http://creativecommons.org/licenses/by/4.0/>).

1. Introduction

Mineral dust (hereafter referred to as dust for short) is a major component of atmospheric aerosols, originating mainly from arid and semi-arid deserts, dry lake beds, and areas with extreme soil moisture deficits and reduced vegetation cover (Chooari et al., 2014). Once aloft, dust aerosols may be carried by winds for long-range transport of an intercontinental scale (Yu et al., 2013), such as the trans-Atlantic transport of North African dust (Chiapello and Moulin, 2002; Yu et al., 2015a, 2015b; Di Biagio et al., 2021), transport of dust plumes from the Arabian Peninsula over the Arabian Sea and the Indian Ocean in summer, and trans-pacific transport of Asia dust in spring (Goudie and Middleton, 2006; Yu et al., 2012). Meanwhile, they can influence the Earth-Atmosphere system's radiative energy budget and thermodynamic structure through aerosol-radiation interactions (ARI). Different from most other aerosol types that are small in size (diameter $\leq 1 \mu\text{m}$), the mass of dust particles is dominated by the coarse mode (diameter $> 1 \mu\text{m}$). Over dark oceans, the scattering effect of dust dominates its interactions with shortwave solar radiation (referred to as "SW"), leading to a negative (i.e., cooling) SW direct radiative effect (DRE_{SW}) at the top of atmosphere (TOA). Due to the predominant coarse mode particle size, dust also has significant radiative effects in the longwave (referred to as "LW"), where the absorption effect is dominant, resulting in a positive (i.e., warming) LW DRE (DRE_{LW}) (Torres et al., 1998; Yu et al., 2006). The net radiative effect of dust, as the sum of DRE_{SW} and DRE_{LW} , has significant impacts on the planetary energy balance (Tegen et al., 1996; Yu et al., 2006; Song et al., 2018), as well as regional weather and climate variability (Tegen and Lacis, 1996; Evan et al., 2006). Despite this qualitative understanding, quantitative estimates of dust DRE remain highly uncertain. Several recent studies argued that most global climate models (GCMs) tend to underestimate the fraction of coarse dust particles that has been observed in the atmosphere (Adebisi and Kok, 2020; Kok et al., 2017; Ryder et al., 2013b). As a result, GCMs overestimate dust DRE_{SW} and underestimate DRE_{LW} (Kok et al., 2017; Di Biagio et al., 2020). In addition to the DRE, dust can also alter various micro- and macro-physical properties of clouds and their evolution and lifetime through aerosol-cloud interactions (ACI) (Li et al., 2019; Wang et al., 2010). Moreover, dust storms and plumes can degrade air quality and generate adverse impacts on human health (Griffin, 2007; Querol et al., 2019).

To better quantify the influences of dust on radiation and clouds, we need continuous observations of dust spatial and vertical distribution and key optical and microphysical properties. The aerosol optical depth (AOD) of dust (DAOD) is fundamental for quantifying the impact of dust through ARI (Gkikas et al., 2018; Song et al., 2018; Thorsen et al., 2020). Presently, satellite-based remote sensing is the only way to obtain such observations on a regional or global scale. Over the last few decades, numerous techniques have been developed to retrieve aerosol properties, in particular the AOD, from satellite observations, such as the Moderate Resolution Imaging Spectroradiometer (MODIS), the multi-angle imaging spectroradiometer (MISR), the Visible Infrared Imaging Radiometer Suite (VIIRS), the Cloud-Aerosol Lidar with Orthogonal Polarization (CALIOP) and the Cloud-Aerosol Transport System (CATS). Most of these techniques operate in the visible (referred to as "VIS") to near-infrared spectral region because most aerosols, such as smoke and industrial pollution, only exert discernable radiative effects in the VIS (Satheesh and Moorthy, 2005). However, as mentioned above, with a large amount of coarse particles, dust also interacts with radiation in the thermal infrared (referred to as "TIR" for brevity) spectral region, allowing for the retrieval of DAOD based on TIR observations (Sokolik et al., 1998).

Satellite-based retrievals of the DAOD in TIR (i.e., DAOD_{TIR}) are essential and highly useful for many purposes. First, the VIS retrieval requires solar illumination and is therefore only available during the daytime. In contrast, the TIR retrieval does not have such limitations, available at both daytime and nighttime. Second, as shown in Capelle

et al. (2014), merely extrapolating the retrieved AOD in VIS to TIR without strong observational constraint can lead to substantial error and uncertainty. Therefore, with a better satellite-based dust TIR retrieval, the dust extinction spectrum from VIS to TIR can be improved by connecting the retrieval from both spectra (Kluser et al., 2012). Third, the DRE_{LW} of dust is more sensitive to the coarse mode of the dust and, therefore, more directly connected to the DAOD_{TIR} rather than the DAOD_{VIS} (Capelle et al., 2014; Peyridieu et al., 2010). For example, Song et al. (2018) showed that two dust models, one with a larger size and less absorptive VIS refractive index, and the other with a smaller size and more absorptive VIS refractive index, can have almost identical DRE_{SW} for a given DAOD_{VIS} . However, the two have quite different DRE_{LW} because of the difference in DAOD_{TIR} extrapolated based on the assumed dust models, attesting to the need for observation-based retrievals of DAOD_{TIR} .

Although satellite based TIR observations are abundant, quantitative retrievals of the TIR dust optical properties are still limited compared to the VIS products due to two major challenges. First, the radiative signal of dust in the TIR is generally weaker due to the relatively small DAOD_{TIR} compared with, for example, clouds. As a result, the noise from atmospheric absorptions in TIR can lead to significant DAOD_{TIR} retrieval uncertainties. The second challenge is that a reliable TIR-based retrieval of DAOD requires precise characterization of the dust layer's vertical location and corresponding temperature profile. For these reasons, most of the current DAOD_{TIR} retrievals are based on observations from hyperspectral sounders, such as the Infrared Atmospheric Sounding Interferometer (IASI) and the Atmospheric Infra-Red Sounder (AIRS) (Kluser et al., 2011; Peyridieu et al., 2010; Xia et al., 2004). The high spectral resolution of these instruments allows for careful channel selection in atmospheric window bands to achieve a better signal-to-noise ratio for the retrieval. The observed spectra also provide enough information content to retrieve both DAOD_{TIR} and dust layer's vertical location. For instance, Pierangelo et al. (2004) demonstrated that DAOD at $10 \mu\text{m}$ and dust mean altitude could be retrieved by matching the BT difference between the computed and the observed BT in 8 selected channels. Later, Kluser et al. (2011) modified this method to utilize observed dust TIR spectra from IASI by using the Singular Vector Decomposition (SVD) method to retrieve both DAOD_{TIR} and dust altitude. The 10+ years of IASI-based near-global retrievals of DAOD_{TIR} have proved to be an instrumental dataset for studying dust transport and radiative effects and evaluating dust simulations in climate models (Capelle et al., 2018). Going beyond the DAOD_{TIR} , Cuesta et al. (2015) developed a new method to retrieve dust vertical profile for major dust outbreaks from IASI. Despite these successes, hyperspectral-based dust retrievals also face several challenges and limitations. First, hyperspectral sounders usually have a coarser spatial resolution (e.g., IASI $\sim 12 \text{ km}$) than TIR imagers (e.g., IIR $\sim 1 \text{ km}$ resolution). At the scale of 12 km , a large fraction of their observations could be contaminated by sub-pixel clouds and thereby overestimated the dust extinction signal (Kaplan, 2013; Martins et al., 2002; Xia et al., 2004). Secondly, the retrieval of dust altitude is usually less accurate than what can be achieved by active sensors such as CALIOP and CATS. The inaccurate dust vertical height would, in turn, affect the accuracy of DAOD_{TIR} retrieval. Moreover, the development of a hyperspectral retrieval algorithm usually involves numerous spectral bands, which can be rather challenging.

This paper explores an alternative method to retrieve nighttime DAOD_{TIR} over oceans based on the integrated observations from CALIOP and IIR onboard the CALIPSO spacecraft. As an active lidar, CALIOP provides accurate information on the vertical location of dust and cloud layer. The IIR provides observations in three TIR bands, from one of which (i.e., Band at $10.6 \mu\text{m}$) the DAOD_{TIR} is retrieved in this study. In comparison with the hyperspectral-based methods, our algorithm has several unique advantages. First of all, the high sensitivity of CALIOP to clouds and the fine spatial resolution of IIR (i.e., 1 km) enables a better cloud masking to avoid potential contamination by sub-pixel clouds. Second, as explained later, the unique depolarization observation of

CALIOP provides a way to detect a dust layer and specify its vertical profile. With these advantages, the DAOD_{TIR} can be retrieved from a single IIR band using a relatively simple algorithm, although a few a priori assumptions of dust properties, such as dust particle size, shape and complex refractive index, are needed. In the rest of this paper, we introduce the integrated IIR/CALIOP observation and the radiative transfer model in Section 2. The implementation of the DAOD_{TIR} retrieval algorithm is explained in Section 3. Section 4 shows the spatiotemporal patterns of the retrieval results and the comparison with IASI retrievals and ground-based AERONET measurement, followed by the summaries and conclusions in Section 5.

2. Data and model

2.1. CALIOP and IIR observations

The CALIOP level-2 retrieval algorithm detects aerosol layers and records their top and bottom heights and layer integrated properties using a “feature finder” algorithm and cloud-aerosol discrimination (CAD) algorithm (Kim et al., 2018; Liu et al., 2019; Liu et al., 2009). The extinction of an identified aerosol layer is then derived from the attenuated backscatter profile using a priori extinction-to-backscatter ratios (i.e., lidar ratios) based on aerosol sub-types (Young et al., 2018; Young et al., 2013). The aerosol sub-type is determined based on the estimated particulate depolarization ratio (DPR), the color ratio, the layer attenuated backscatter, and the detected aerosol layers height (Kim et al., 2018). Note that the CALIOP operational aerosol product does not provide the specific dust extinction profile when dust is mixed with other types of aerosols (e.g., polluted dust and dusty marine). To alleviate this issue, instead of using the aerosol sub-type information, we mainly use the DPR along with the CAD score from the Version-4 Level-2 CALIOP aerosol profile product (“LID_L2_05kmAPro-Standard-V4”) to estimate the portion of the attenuated backscatter profiles contributed by dust aerosols, and then to obtain the dust aerosol extinction profiles and column DAOD (see Section 3.2 for detail). The derived dust aerosol extinction profiles further serve as the dust aerosol vertical distribution for the DAOD_{TIR} retrieval.

The IIR provides measurements of the upwelling radiances in three TIR channels centered around 8.65, 10.6, and 12.05 μm with a medium spectral resolution of 0.9, 0.6, and 1.0 μm , respectively. The instantaneous field of view of IIR is 64 km \times 64 km with a pixel size of 1 km by 1 km centered on the CALIOP ground track. The instrument is regularly calibrated using images from cold (about 4 K) deep-space views and a warm blackbody source of 25°C. The calibrated radiances reported in the IIR Level 1b product are further represented by equivalent brightness temperatures (BTs) computed using Planck’s law and the relevant instrument spectral response functions (SRF) (see Fig. 5 (black dash lines)) in the Level 2 product. Recent updates of the calibration corrected the residual systematic bias in the northern hemisphere. A detailed introduction of the IIR instrument and its calibration process is shown in Garnier et al. (2018). The noise equivalent differential temperature and calibration accuracy was assessed by the Centre National d’Etudes Spatiales (CNES) (Garnier et al., 2012). The instrument exhibits an intrinsic 1-sigma noise equivalent to 0.2–0.3 K for a scene temperature of 210 K that improves to 0.1–0.15 K at 250 K and above (see Table 1 in Garnier et al., 2012). In this study, the cloud-free dust-laden cases are rarely lower than 250 K. Taking the calibration short term instability (0.1 K) into account, we estimated random measurement uncertainties for each 1-km IIR pixel with ± 0.15 K, ± 0.2 K and ± 0.17 K in the three IIR channels, respectively.

Table 1 lists all variables with the specific values from the Version 4 Level-2 CALIOP aerosol profile product and the Version 4 Level-2 IIR along-track product (“IIR_L2_Track-Standard-V4”) used in this study. Beyond the BT measurements, the IIR_L2_Track-Standard-V4 product also provides a background reference flag (defined as “Was_Cleared_Flag_1km”) to report the number of clouds seen by the 1-km IIR pixel

Table 1

Variables of level-2 CALIOP and IIR products that are used in this study.

Products	Variable	Value is used
IIR_L2_Track-Standard-V4	Type_of_scene	Cloud-free clean sky (10)
	Was_Cleared_Flag_1km	No single-shot cloud (0)
	TGeotype	Open Water (1700)
	Brightness_Temperature	All
	Surface_Emissivity	Ocean only (0.971, 0.984, 0.982 at 8.65, 10.6, 12.05 μm)
	IIR_Data_Quality_Flag	Calibrated radiances (0)
	CAD_score	–100 < CAD < –90
	Particulate_Depolarization_Ratio_Profile_532	All
	Particulate_Depolarization_Ratio_Uncertainty_532	< 0.18
	Extinction_QC_Flag_532	0,1,16,18
LID_L2_05kmAPro-Standard-V4	Total_Backscatter_Coefficient_532	All
	Atmospheric_Volume_Description	Feature types for cloud detection

that CALIOP also detected at single-shot resolution (i.e., 333 m) but that were cleared from the CALIOP 5-km layer products to improve the detection of aerosols at coarser spatial resolutions (Vaughan et al., 2005). It helps identify confident cloud-free aerosol profiles for the derivation of the vertical distribution of dust extinction. The LID_L2_05kmAPro-Standard-V4 product has a 5-km along-track spatial resolution, while the IIR_L2_Track-Standard-V4 product is in 1-km resolution. To match these two datasets, we match the 5-km CALIOP segments to five successive 1-km IIR footprints.

2.2. The radiative transfer models and reanalysis data

The backbone of our DAOD_{TIR} retrieval algorithm is the FAST radiative transfer code with the Discrete Ordinate Method (FASDOM) developed by Dubuisson et al. (2005). This radiative transfer model (RTM) uses the correlated k -distribution method tailored to the IIR SRFs to calculate the atmospheric gas absorptions. With a full account for multiple scattering, the radiative transfer equation is solved by the coupled discrete ordinate radiative transfer code (DISORT) developed by Stamnes et al. (1988). The inputs into FASDOM code include atmospheric profiles (temperature, water vapor and ozone), surface temperature, surface emissivity, aerosol layer location in atmospheric profiles, aerosol layer optical depth (OD) and spectral radiative properties (i.e., single-scattering albedo and asymmetry factor). The FASDOM code has been thoroughly evaluated by comparing the combined line-by-line and DISORT radiative transfer code. Simulations have shown that the accuracy is generally better than 0.3 K for BT (Dubuisson et al., 2005; Dubuisson et al., 2008).

Implementing the radiative transfer simulation for global satellite observations requires a reliable dataset of atmospheric states with relatively high spatial and temporal resolution. In this study, we use the instantaneous assimilated atmospheric profiles and surface temperature from Version 2 Modern-Era Retrospective analysis for Research and Applications (MERRA-2) as RTMs’ input. The atmospheric profiles from MERRA-2 “inst3_3d_asm_Nv” product have a gridded horizontal

resolution of 0.5° latitude \times 0.625° longitude and 72 pressure levels from the surface to 0.01 hPa with a 3-h time step. The surface temperature from “inst1_2d_asm_Nx” product shares the exact horizontal resolution with a 1-h time step. Detailed information is provided in Gelaro et al. (2017). For each IIR-CALIP observation with the geolocation that falls within a grid box of MERRA-2 data, the observation time is used to find the closest time step of MERRA-2 data. Afterward, the corresponding atmospheric profiles and surface temperature of the matched grid box with the matched time step are used as the input for FASDOM.

As explained later in Section 3.3, the retrieval of DAOD_{TIR} relies on the difference of brightness temperature (BT) at TOA between the cloud-free clean atmosphere (referred to as “ BT_{clean} ”) and the cloud-free dusty atmosphere (referred to as “ BT_{dust} ”). Thus, an accurate estimate of BT_{clean} is a prerequisite for the accurate retrieval of DAOD_{TIR} . In this regard, the algorithms based on hyperspectral observations have an obvious advantage, i.e., they can select channels in atmospheric window bands to reduce the impacts of atmospheric profile uncertainties. In contrast, the much broader spectral response of IIR bands makes them more susceptible to atmospheric profile uncertainties. To understand the magnitude and impacts of this uncertainty, we performed a careful radiative closure benchmark study. First, we used the “cloud-free clean” scene type in the “IIR_L2_Track-Standard-V4” product to select those cloud-free and low-aerosol-loading profiles. Ideally, without the impact of cloud or aerosol, the simulated BT_{clean} based on MERRA-2 atmospheric profiles and FASDOM should agree with the observed BT_{clean} . Of course, they could differ significantly in reality because of various uncertainties, including instrument noise, uncertainty in MERRA-2 profile, and/or radiative transfer error. Therefore, the difference between simulated and observed BT_{clean} provides us a reasonable estimate of the impacts of these critical uncertainty sources on our dBT LUT. The results from this radiative closure study are shown in Fig. 1.

The radiative closure over land has a large discrepancy (up to ± 10 K) because of the high-varied surface emissivity and skin temperature around the TIR window spectrum over bright deserts (Zhou et al., 2013). Thus, in this study, we only consider retrieval over the ocean and mask out the land regions. In addition, to focus on the simulation performance over the dust-concentrated region, the derived 2-year annual CALIP DAOD

at 532 nm (referred to as “ $\text{DAOD}_{532\text{nm}}$ ”; the derivation process is explained in Section 3.2) from 2007 to 2008 is used to define the area with noticeable dust loadings for the radiative closure testing. As shown in Fig. 1a, the area with DAOD larger than 0.03 generally covers the “global dust belt” extending from the tropical Atlantic northeastward to the northwestern Pacific (roughly from 0° to 50°N and from 60°W to 150°E) (Song et al., 2021; Xu et al., 2018; Yu et al., 2010; Yu et al., 2020). Therefore, we define this area as the dust-concentrated region over oceans.

Fig. 1b–d show the BT_{clean} difference between IIR and FASDOM (referred to as “ $\text{dBT}_{\text{clean}}$ ”) is within ± 2.0 K at all three IIR bands. Out of the dust-concentrated region, the $\text{dBT}_{\text{clean}}$ has a positive bias, especially in the Southern Ocean. Although the cause of this bias is not fully understood, it could be a combination of several factors, including biases in MERRA-2 data and/or issues in radiative transfer models. However, the radiative closure results over the dust-concentrated region are highly encouraging, i.e., with the annual mean difference primarily within ± 0.1 K, indicating a good agreement between simulated and observed BT_{clean} . Fig. 2 provides a more quantitative perspective by separating the daytime and the nighttime cases over the dust-concentrated region. As shown in Fig. 2b, the probability distribution function (PDF) of $\text{dBT}_{\text{clean}}$ over the dust-concentrated region for all three IIR bands follows a Gaussian-shape distribution for nighttime cases with the peak centered around zero (biases smaller than 0.05 K). However, the daytime cases in Fig. 2a have a 0.25 K positive bias and ~ 0.15 K larger standard deviations. Similar bias in daytime is found and discussed in previous studies for both IIR and MODIS (Garnier et al., 2021; Garnier et al., 2017). The exact reason for the slight but systematic bias in daytime cases remains unclear. Thus, we only use nighttime observations for the DAOD_{TIR} retrieval in this study. Note that the random error of IIR measurement with 0.2 K is already included throughout the radiative closure benchmark. Therefore, the uncertainty from both observations and forward simulations can be represented by one standard deviation of the BT_{clean} difference at each IIR channel.

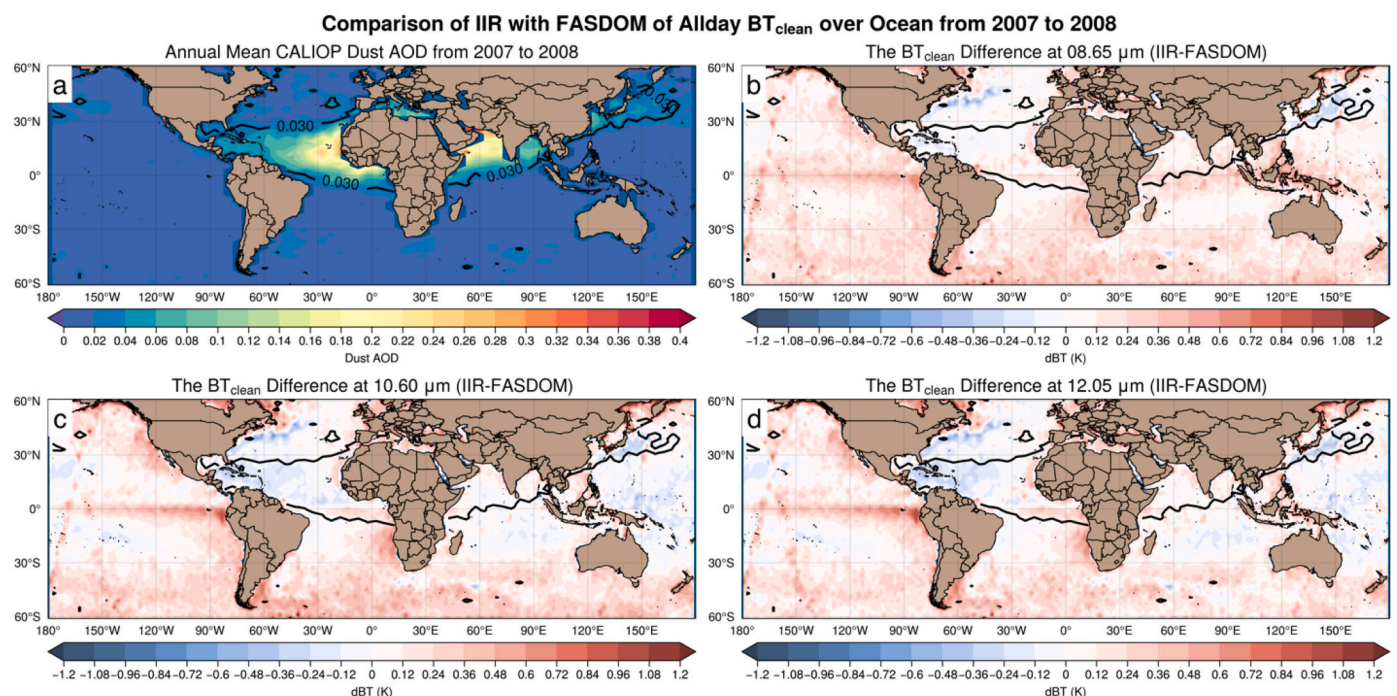


Fig. 1. The global distribution of the annual mean CALIP DAOD (a), the BT_{clean} difference of all-day $\text{dBT}_{\text{clean}}$ (IIR-FASDOM) at 8.65 μm (b), 10.60 μm (c) and 12.05 μm (d) over oceans from 2007 to 2008. The black contour line represents the annual mean CALIP DAOD of 0.03 from 2007 to 2008.

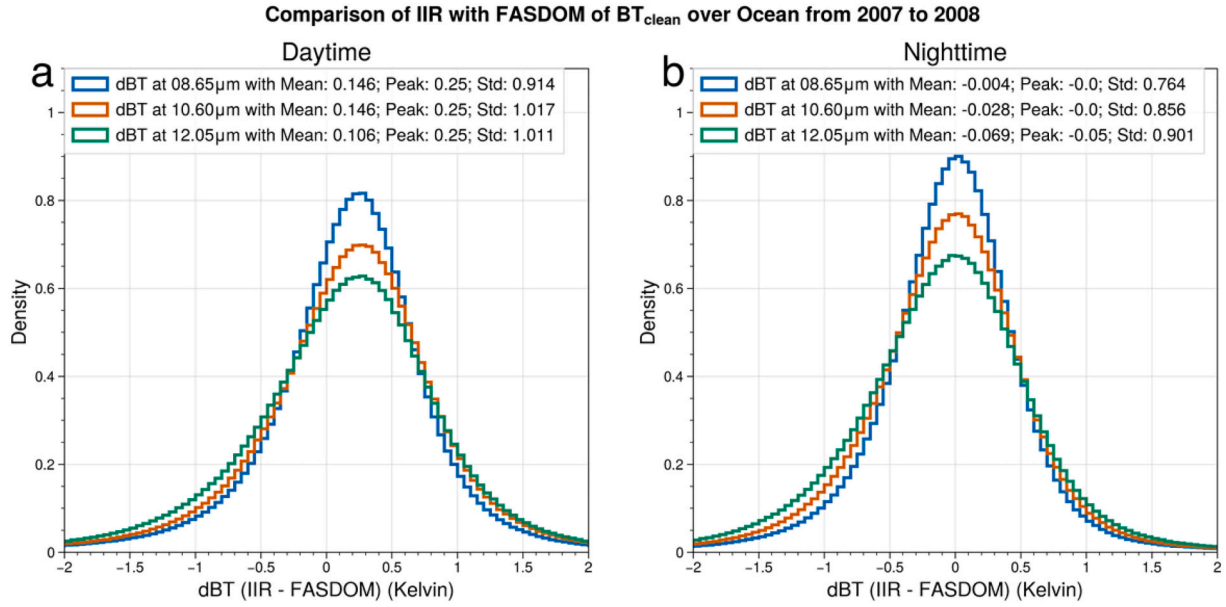


Fig. 2. The probability distribution function (PDF) of daytime (a) and nighttime (b) dBT (IIR-FASDOM) of BT_{clean} at 8.65 μm , 10.6 μm and 12.05 μm over oceans from 2007 to 2008 for the dust-concentrated region as indicated in Fig. 1.

3. Description of retrieval algorithm

3.1. The use of 10.6 μm channel for $DAOD_{TIR}$ retrieval over ocean

Although IIR has three bands with similar observational uncertainties as analyzed above, we choose to use only the 10.6 μm channel for the $DAOD_{TIR}$ retrieval over oceans during nighttime based on the following considerations. First, as will be shown later in Fig. 5 (Section 3.3), as well as in the atmospheric transmission spectrum (Dubuisson et al., 2005), the 10.6 μm channel contains a more extensive dust extinction and with higher atmospheric transmission than the other two channels, which means a better signal-to-noise ratio for the $DAOD_{TIR}$ retrieval. Secondly, as previous studies usually report the $DAOD_{TIR}$ retrieval results at around 10 μm (Capelle et al., 2014; Peyridieu et al., 2010), the choice of 10.6 μm channel will facilitate comparisons of our results with these previous estimates. Finally, although the three IIR channels provide independent observations, they share similar BT differences due to the change of DAOD at their spectral range (see Fig. A4 in Capelle et al. (2014)), leading to insufficient information content regarding the spectral BT difference among the three IIR channels. Note that we can use a single channel to retrieve the $DAOD_{TIR}$ because CALIOP specifies the vertical distribution of dust. In contrast, hyperspectral IR observations need information at different wavelengths to simultaneously retrieve $DAOD_{TIR}$ and mean dust altitude as the dust layer height has the same order-of-magnitude of information content as $DAOD_{TIR}$ (Kluser et al., 2015; Xia et al., 2004).

Although the use of a single channel makes the $DAOD_{TIR}$ retrieval algorithm relatively straightforward, it necessitates assumptions of dust properties, such as dust size, shape and complex refractive index. Although this is a common practice in aerosol remote sensing due to the lack of information, the pre-assumed properties inevitably fall short of the variability of actual dust and therefore may lead to retrieval uncertainties. We test the sensitivity of the pre-assumed dust particle size and complex refractive index in our retrieval and analyze their contribution to retrieval uncertainties in Sections 3.5 and 3.6. In future research, we will also explore the possibility of retrieving other dust properties in addition to $DAOD_{TIR}$ using more IIR channels and/or other IR observations from MODIS and AIRS.

3.2. Cloud masking and dust detection

An essential prerequisite for a successful $DAOD_{TIR}$ retrieval is reliable identification of cloud-free and dust-laden profiles and pre-knowledge of the vertical distribution of dust within the profile. This step of cloud masking and dust detection can be challenging for passive sensors with relatively coarse spatial resolution (e.g., AIRS and IASI). But the unique capabilities of CALIOP, together with the supplementary information from IIR, make this step relatively straightforward, as explained below.

We use the 5-km “LID_L2_05kmAPro-Standard-V4” product from CALIOP and the 1-km “IIR_L2_Track-Standard-V4” product from IIR. As aforementioned, the 5-km CALIOP segments are first collocated with the 1-km IIR pixels so that each CALIOP profile contains five IIR pixels.

Cloud screening is done in two steps using the two collocated products. In the first step, we use the vertical features mask (“Atmospheric_Volume_Description”) from the “LID_L2_05kmAPro-Standard-V4” product to filter out any 5-km profiles that contain cloud layers or stratospheric aerosol. It should be noted that even after the first step screening, ~59% of the remaining CALIOP 5-km segments are still partly cloudy (i.e., containing sub-pixel clouds, see Table 2). It results from the “hiding” single-shot cloud in the 5-km CALIOP segments. Therefore, in the second step of cloud masking, we use the “Was_Cleared_Flag_1km” to find the cloud-free 1-km IIR pixels within

Table 2

The pre- and post-quality control flags assigned in the retrieval process.

QA flag	Value	Description	Number of Samples in 2013 (total: 1888273)
pre_QA	0	All 1-km pixels in a 5-km profile are cloud-free aerosol	767,040 (40.62%)
	1	Part of 1-km pixels in a 5-km profile are cloud-free aerosol	828,445 (43.87%)
	2	None of 1-km pixels in a 5-km profile are cloud-free aerosol	292,788 (15.51%)
post_QA	0	retrieved DAOD / CALIOP DAOD < 2.0	1,796,767 (95.16%)
	1	retrieved DAOD / CALIOP DAOD ≥ 2.0	59,013 (3.12%)
	2	A 5-km profile with dBT ($BT_{dust} - BT_{clean}$) > 0	32,493 (1.72%)

those partly cloudy 5-km CALIOP pixels and assign them pre-quality assurance (pre_QA) flags with descriptions in Table 2. Note that the assignments of the post-quality assurance (post_QA) flags are further explained in Section 3.6.

After cloud masking, the next step is to identify dust and specify its vertical profile. As the first step of dust detection, we use the extinction control flag ("Extinction_QC_Flag_532") in the CALIOP product to select only reliable retrievals (i.e., Extinction_QC_Flag_532 = 0, 1, 16 or 18 (Winker et al., 2013; Yu et al., 2015a)). Previous studies pointed out that the optically dense dust was frequently mis-identified as thin cloud by Version 2 cloud-aerosol discrimination (CAD) algorithm (Chen et al., 2010; Chen et al., 2014). However, by taking the layer-integrated volume DPR and the feature latitude into account, the Version 3 and 4 CAD algorithms significantly improved the performance of aerosol detection (Liu et al., 2010). Therefore, we further select from the remaining profiles with the cloud-aerosol discrimination (CAD) score between -100 and -90 to ensure the detected feature is aerosol with high confidence (Liu et al., 2009; Yu et al., 2019).

As mentioned in Section 2.1, the extinction profile classified as polluted dust and dusty marine from the V4 CALIOP operational product contains the dust mixture with other non-dust aerosols, such as industrial pollution, biomass burning smoke, and marine aerosols. Most of the non-dust aerosols have little extinction in the TIR region due to their small size, except marine aerosols that have a comparable size distribution with dust (Sayer et al., 2012). Nonetheless, marine aerosols are mainly concentrated within the marine boundary layer with relatively low SW AOD (of the order of 0.1) and thus have limited impact on the outgoing longwave radiation (OLR) at TOA (Xia et al., 2004).

Consequently, for our DAOD_{TIR} retrieval, we need to know the vertical profile of only dust aerosols. For this purpose, we apply a widely used technique to first derive a vertically resolved fraction of dust backscatter (β_d) to total backscatter (β), i.e., $f_d(z) = \beta_d(z)/\beta(z)$ from the following equation:

$$f_d(z) = \frac{(\delta(z) - \delta_{nd})(1 + \delta_d)}{(1 + \delta(z))(\delta_d - \delta_{nd})} \quad (1)$$

where $\delta(z)$, δ_d and δ_{nd} are the observed particulate DPR from CALIOP, pre-assumed particulate DPR of dust and non-dust aerosols, respectively. Following Yu et al. (2015a), the lower and upper limits of δ_{nd} are set to 0.02 and 0.07 and δ_d to 0.20 and 0.30, respectively. The f_d upper bound is estimated based on the combination of $\delta_d = 0.2$ and $\delta_{nd} = 0.02$ and the lower bound based on $\delta_d = 0.3$ and $\delta_{nd} = 0.07$. The value of f_d is set to be 1 when $f_d > 1$ and 0 when $f_d < 0$. For simplicity, the final f_d is set to the mean value of the upper and lower bounds. Lastly, using the derived f_d and pre-assumed lidar ratio for pure dust, i.e., $S_d = 44$ sr at 532 nm, we convert the aerosol backscatter profile ($\beta(z)$) from the CALIOP aerosol profile product to dust extinction profile $\sigma_d(z) = S_d \cdot f_d(z) \cdot \beta(z)$, and further the DAOD_{532nm} from the column σ_d . It is important to note that the $\sigma_d(z)$ is used for scaling the input layer OD with a given DAOD_{TIR} in FASDOM to represent the vertical distribution of dust. In other words, the assumption of S_d is irrelevant on the DAOD_{TIR} retrieval but impacts the absolute value of CALIOP DAOD_{532nm}. Moreover, we assume that the dust properties, e.g., size and refractive index, are the same within a dust layer. This assumption may lead to uncertainties as dust particles could become stratified during transport because of vertical sedimentation processes (Yang et al., 2012). However, numerous studies suggest that the dust particle size and shape do not change noticeably during the cross-ocean transport (Christopher and Jones, 2010; Maring et al., 2003; Peyridieu et al., 2013). We leave the investigation of this uncertainty to future research and assume it is a second-degree level compared to other sources, e.g., radiative transfer modeling, dust size and dust refractive index.

The corresponding cloud-free 1-km IIR BTs are eventually averaged back to 5 km footprints. For example, if a partly cloudy 5-km CALIOP pixel has three cloud-free 1-km IIR pixels, then the input BTs for the

DAOD_{TIR} retrieval is based on the mean value of the three cloud-free IIR pixels. The retrieval results are, therefore, in 5 km spatial resolution along the CALIOP track.

3.3. A priori assumption of dust optical properties

The single band (i.e., 10.6 μ m) DAOD_{TIR} retrieval requires dust properties other than the dust altitude to be pre-assumed. This section introduces the dust particle size distribution (PSD), dust shapes, and dust complex refractive index (RI) that are used to derive the dust bulk scattering properties, including the extinction efficiency (Q_{ext}), single-scattering albedo (SSA) and asymmetry factor (g-factor).

As the retrieval is implemented over oceans only, it needs appropriate a priori dust PSDs obtained at dust-transport areas. Hence, we retrieve and report two sets of DAOD_{TIR} retrievals based on two pre-assumed dust PSDs; as introduced further below, one is retrieved by AERONET measurements at Cape Verde (Dubovik et al., 2002), and the other is observed in the Saharan Air Layer during the Fennec 2011 aircraft campaign (Ryder et al., 2013b). Song et al. (2018) used these two dust PSD to compute dust DRE over the tropical North Atlantic. Their result shows a remarkable difference of simulated DRE_{LW} based on these two PSDs. Without the observational record in TIR, it is reasonable to have extrapolated DAOD_{TIR} and, therefore, DRE_{LW} based on the same DAOD_{VIS} but different PSDs, especially in the coarse mode. Therefore, it is worth showing if similar impacts of dust particle size occur on the DAOD_{TIR} retrieval.

The first PSD is based on AERONET climatology at Cape Verde (16°N, 22°W) (referred to as "AERONET" PSD) averaged from 1993 to 2000 by Dubovik et al. (2002) to represent the transported dust PSD as it is from a dust-dominant site (Gama et al., 2015; Mahowald et al., 2014; Song et al., 2018). Note that the PSD retrieval artifact of AERONET measurements due to dust non-sphericity was corrected in our use of the AERONET PSD (Dubovik et al., 2002). Details of the AERONET PSD retrieval process can be found in Dubovik et al. (2000). The second set of dust PSD is taken from the Fennec field campaign during June 2011 over the eastern Atlantic Ocean, which is categorized as the airborne dust within the Saharan Air Layer (SAL) (referred to as "Fennec" PSD). This category is from the average of vertical profile observations excluding the marine boundary layer. It represents the airborne dust transported over the nearby eastern Atlantic Ocean with the remarkably disclosed larger particle sizes than measured previously in dust layers, as well as the AERONET PSD (see Fig. 3). The errors due to sizing uncertainties have also explicitly been quantified (see Ryder et al. (2013a) for details).

Fig. 3 shows the normalized volume size distribution of AERONET PSD and Fennec PSD as the visual comparison. The coarse mode of AERONET PSD has the peak with diameter around 3 μ m, while the diameter of the peak of Fennec PSD is larger than 10 μ m. As the fine-mode PSD rarely (~10%) changes the dust extinction in TIR (Pierangelo et al., 2013), the difference of the coarse mode between the two PSDs mainly impacts the DAOD_{TIR} retrieval.

For the dust RI, we use a state-of-art database developed by Di Biagio et al. (2017) (referred to as "Di-Biagio" database). It has laboratory measured RIs for dust aerosols generated from natural soil samples collected in 19 arid and semi-arid sites from 8 regions globally, including northern Africa, the Sahel, eastern Africa and the Middle East, Eastern Asia, North and South America, southern Africa, and Australia. Compared with other older dust RI databases in the literature, e.g., Volz (1973) and OPAC (Hess et al., 1998), the Di-Biagio database is more comprehensive and allows for the choice of regional dependent RI for DAOD_{TIR} retrieval. As shown in Fig. 4, in our algorithm, we divide the global ocean into seven regions and then assign one or more regional RI from the Di-Biagio database based on the dust transport model simulations (Griffin, 2007; Querol et al., 2019). For each 5-km IIR pixel, we take the ensemble of RI for the region of influence and average the retrieved DAOD_{TIR} corresponding to each assigned RI. Although this is a simplified approach, it still helps us capture the variability of dust RI to a

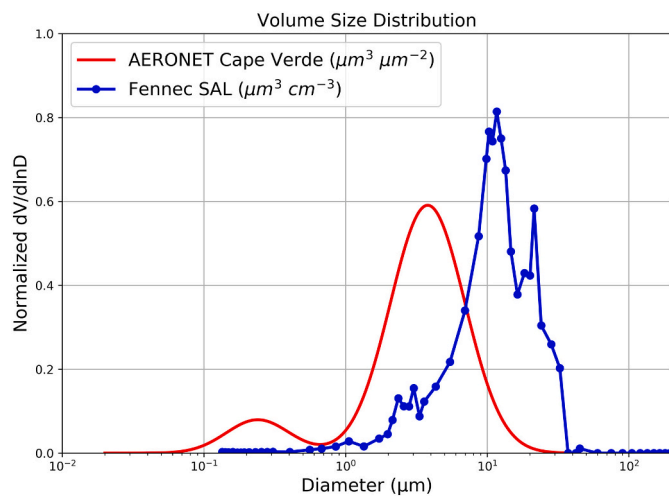


Fig. 3. The size-normalized dust volume PSD. The red curve represents the PSD retrieved from AERONET measurements at Cape Verde reported in Dubovik et al. (2002). The blue dot curve represents the PSD obtained from airborne measurement during Fennec campaign during June 2011 over the eastern Atlantic Ocean (Ryder et al., 2013a). (For interpretation of the references to color in this figure legend, the reader is referred to the web version of this article.)

certain extent. Moreover, as explained in Section 3.4, the sensitivity of regional RIs to the radiative signal of dust at the IIR 10.6 μm channel is relatively low.

For dust shape, studies on their impact on scattering properties have proved that spheroid assumption is a reasonable first-order approximation of the shape of non-spherical dust (Dubovik et al., 2006; Mishchenko et al., 1997). Consequently, we assumed a spheroid shape of dust particles with the size-independent aspect ratio distribution from Dubovik et al. (2006).

Dust bulk scattering properties (i.e., Q_{ext} , SSA and g-factor) for the different combinations of dust PSDs, RIs and shapes are calculated using the T-matrix code developed by Mishchenko (2000) as shown in Fig. 5. We also calculate the $Q_{\text{ext,TIR}}/Q_{\text{ext,VIS}}$ (i.e., TIR/VIS) ratio as it is not only the key element to compare DAOD_{TIR} retrievals with observations in VIS

(e.g., CALIOP DAOD; see Section 4.1) but also impacts the DRE_{LV} calculation in climate models (Capelle et al., 2014; Kok et al., 2017). Because the variability of the real part of SW RIs in literature is negligible at 550 nm (Ryder et al., 2019), we use one SW RI (1.53-0.0055i at 550 nm) from the OPAC database to calculate the $Q_{\text{ext,VIS}}$ with the given dust PSDs.

In the plots, red and blue color groups correspond to scattering properties based on AERONET and Fennec PSD, respectively. Each color group contains 19 lines corresponding to the 19 RI in the Di-Biagio database. By looking at the difference between two dust PSD groups using the Di-Biagio RIs, one can see, in Fig. 5a, b and d, that the sensitivity of dust size to Q_{ext} , TIR/VIS ratio and g is more significant than that of dust RIs as the groups are completely separated, while the spectral variation of SSA in Fig. 5c in two groups are more entangled. It is because the regional RIs mainly differ in the imaginary parts, while the real parts are almost identical at 10.6 μm (Di Biagio et al., 2017). However, the change of SSA with RI shows a limited impact on the radiative signal of dust, which is discussed in Section 3.4. The grey and black bars in Fig. 5 are the SRF (dash lines with right y-axis) integrated scattering properties centered at 3 IIR bands. Table 3 lists the integrated Q_{ext} , SSA and g-factor based on combinations of the two dust PSDs and the 19 regional dust RIs at 10.6 μm by IIR SRFs. The SSA and g-factor are finally used as the input of dust radiative properties in the FASDOM simulation for retrieving DAOD_{TIR}.

3.4. The retrieval framework

A flow chart of our DAOD_{TIR} retrieval algorithm is given in Fig. 6. With the IIR BT at 10.6 μm for the identified cloud-free dust profiles after the screening process introduced in Section 3.2, the BT difference due to dust (referred to as “dBT”) is then obtained by subtracting the IIR observed BT_{dust} with the FASDOM simulated BT_{clean} using the collocated MERRA-2 assimilated atmospheric profiles (included temperature, water vapor and ozone profiles with height and pressure profiles) and surface properties (included MERRA-2 surface temperature and surface emissivity from IIR Level-2 product). Afterward, with the a priori dust scattering properties calculated based on the assigned regional RIs, dust PSD and shape, and the CALIOP-derived dust vertical distribution, the look-up table (LUT) of dBT as a function of DAOD_{TIR} is built simultaneously for each cloud-free dust profile. Finally, the corresponding

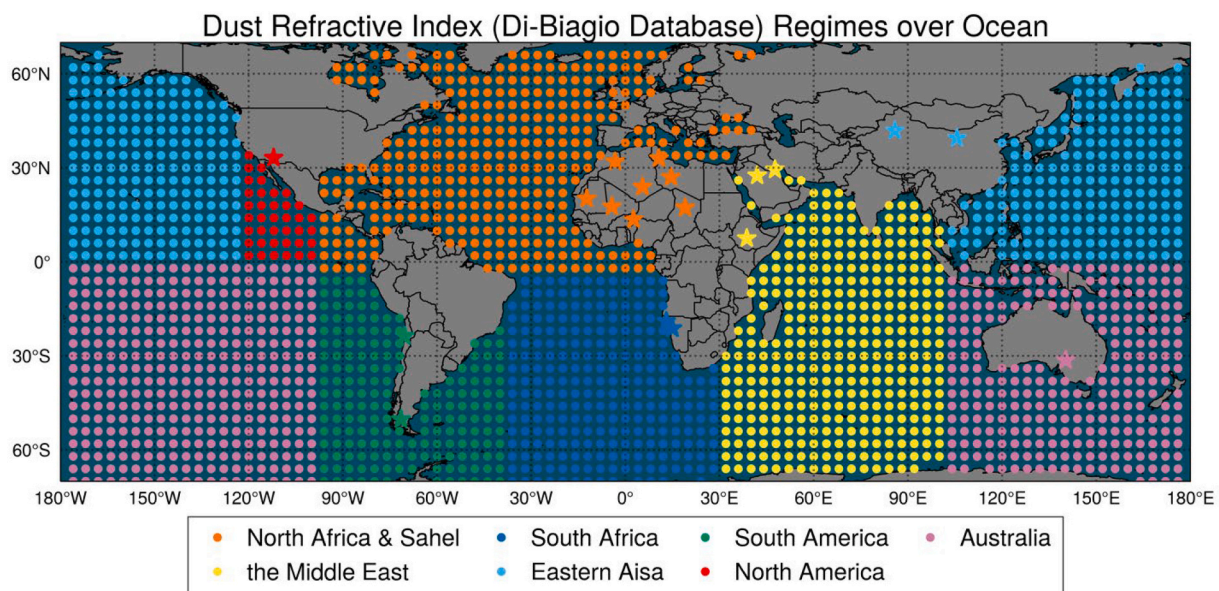


Fig. 4. The assigned seven ocean regimes corresponding to Di-Biagio RIs according to the dust transport simulation in Querol et al. (2019). The stars over land represent the location of the soil and sediment samples collected for the dust RIs. Each color of the stars represents the regime for which it applies.

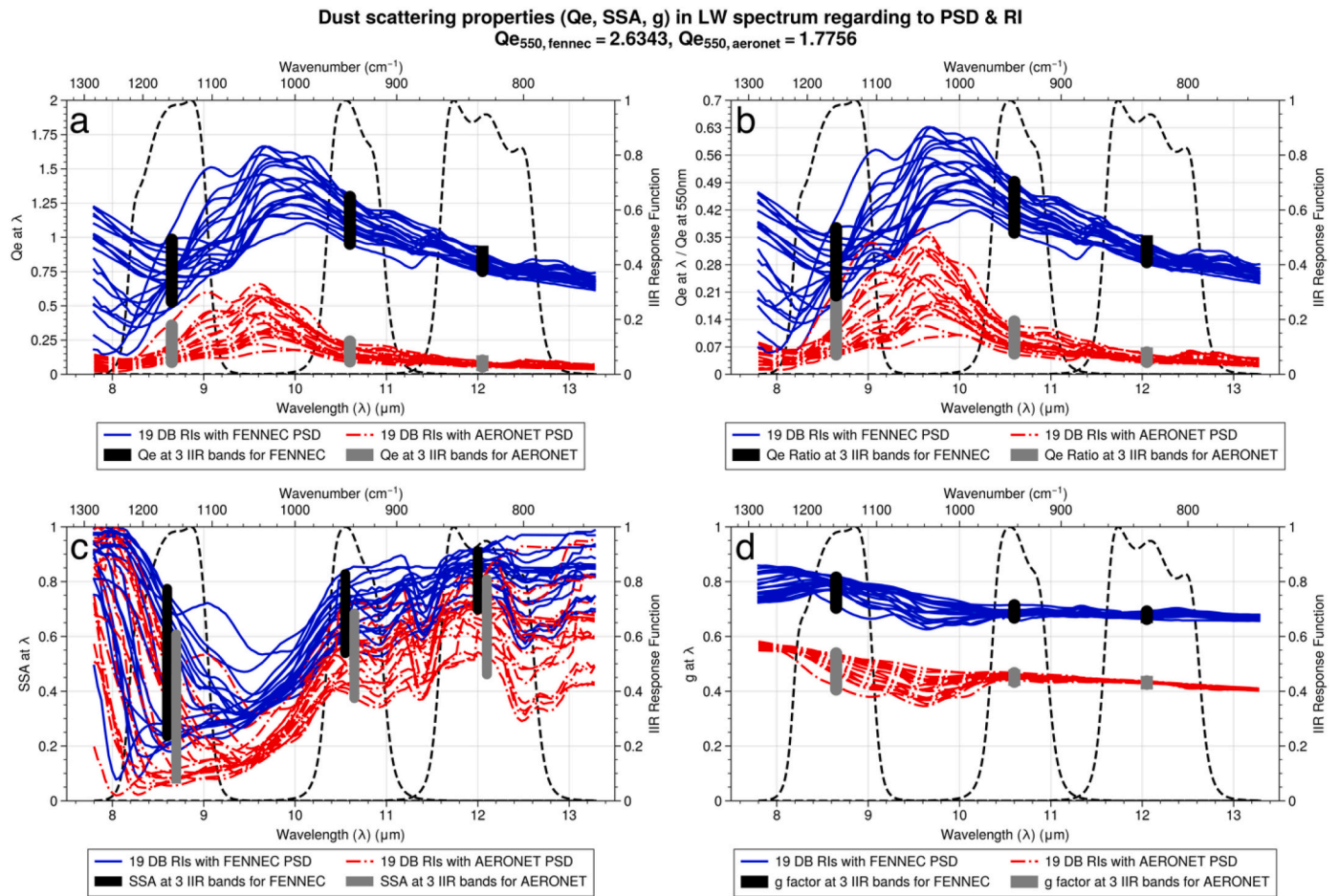


Fig. 5. The scattering properties (Q_{ext} (a), Q_{ext} ratio (b), SSA (c) and g (d)) calculated using the spheroid assumption by T-matrix. The blue lines and red dash-dot lines represent the result calculated by assuming the Fennec PSD and the Aeronet PSD, respectively. Black and grey bars represent the convolved scattering properties using the IIR spectral response functions (SRF) (dash lines with right y-axis) at three bands, respectively (centered at 8.65, 10.6 and 12.05 μm). (For interpretation of the references to color in this figure legend, the reader is referred to the web version of this article.)

DAOD_{TIR} to the matched BT from LUT with the observational IIR BT can be retrieved. The following estimated absolute retrieval uncertainty and the post-screening process are introduced in Section 3.6.

As an illustrative example, we first applied the retrieval framework to a case in Fig. 7. In Fig. 7a, CALIOP observations reveal a dense dust layer from 3 km to 5 km above the ocean surface with some broken marine boundary layer clouds underneath it. Fig. 7b shows the variation of IIR observed BT_{dust} at 10.6 μm and the corresponding BT_{clean} simulated by FASDOM. In this case, the 1-km IIR pixels can capture BT's rapid change due to the marine boundary layer cloud extinction. After applying the dust detection method presented in Section 3.2, the identified cases maximally exclude the observed BT with cloud contaminations (blue dots on top of IIR BT in Fig. 7b). Corresponding to the cloud-free dust cases, Fig. 7c shows the comparison of dBT (IIR BT_{dust} - FASDOM BT_{clean}) with the derived CALIOP DAOD at 532 nm. Evidently, the IIR absolute dBT value has a positive correlation with the CALIOP DAOD for this scene, illustrating the sensitivity of IIR observation to the DAOD_{TIR} retrieval at 10.6 μm . Because the scene is located in the North Atlantic affected by the Africa and Sahel regions in Fig. 4, we use the dust RIs from Sahara and Sahel accordingly, in the calculation. Both Fennec PSD and Aeronet PSD are used to obtain two sets of dust bulk scattering properties for the retrieval. Utilizing the dBT signal, Fig. 7d shows the retrieved DAOD at 10.6 μm (referred to as "DAOD_{10.6 μm "") for the dust with Aeronet PSD (red dot line) and Fennec PSD (blue dot line). We found that the same dBT signal yields larger retrieved DAOD when using Fennec PSD's larger particle size than Aeronet PSD. The}

explanation on this requires further understanding about the impact of bulk scattering properties regarding different dust PSD on the dBT signal, which is discussed in the next section.

3.5. Sensitivity of the retrieval to assumed dust particle size and dust refractive indices

In FASDOM simulation, the variation of the input SSA and g -factor due to the change of dust PSD and RI yields different BT_{dust}, and hence different dBT LUT. In the retrieval framework, with the same observed dBT, the change of LUT leads to different retrieved DAODs corresponding to the change of dust PSD and RI. Therefore, investigating how dust PSD and RI impact the dBT simulation by changing the dust scattering properties (see Fig. 5c and d) helps understand the DAOD_{TIR} retrieval uncertainty caused by the pre-assumed dust properties. The dBT simulation also depends on the atmospheric states, the surface properties, and the dust vertical distribution. To evaluate these factors, we study the sensitivity of dBT at IIR 10.6 μm for two selected cases, one over the subtropical Atlantic Ocean (Fig. 8b) and the other the coastal region near the Sahara Desert (Fig. 8e). Table 4 lists the parameters of the two cases in the sensitivity studies.

In the first case, a long-term transport dust layer is observed between about 2.5 km and 6.3 km by CALIOP (Fig. 8c), with a layer mean temperature around 270 K compared to the warm surface temperature at 301 K (Fig. 8b). In the sensitivity test, we keep the DAOD_{TIR} settled at 0.2 and then use FASDOM to simulate the BT_{dust} and the corresponding dBT

Table 3

The Q_{ext} , SSA and g-factor at 10.6 μm calculated based on the combination of regional RIs over the seven RI regimes with the AERONET PSD and Fennec PSD.

Region	RI	PSD	Q_{ext}	SSA	g-factor
North Africa & Sahel	Algeria	AERONET	0.2103	0.3894	0.4419
		Fennec	1.2289	0.5628	0.6889
	Bodele	AERONET	0.1301	0.5726	0.4594
		Fennec	1.0784	0.7319	0.6909
	Libya	AERONET	0.1417	0.5466	0.4570
		Fennec	1.1130	0.7084	0.6885
	Mali	AERONET	0.2014	0.4544	0.4444
		Fennec	1.2636	0.6103	0.6790
	Mauritania	AERONET	0.1871	0.5146	0.4464
		Fennec	1.2631	0.6704	0.6689
	Morocco	AERONET	0.1452	0.5293	0.4562
		Fennec	1.1149	0.6962	0.6903
	Niger	AERONET	0.1896	0.4684	0.4469
		Fennec	1.2348	0.6253	0.6804
	Tunisia	AERONET	0.1400	0.5445	0.4573
		Fennec	1.1052	0.7089	0.6902
Middle East	Ethiopia	AERONET	0.1104	0.6471	0.4629
		Fennec	1.0279	0.7936	0.6906
	Saudi Arabia	AERONET	0.1338	0.5558	0.4583
		Fennec	1.0806	0.7234	0.6904
	Kuwait	AERONET	0.1389	0.4158	0.4574
		Fennec	0.9962	0.6257	0.714
Eastern Asia	Gobi	AERONET	0.1935	0.4114	0.4456
		Fennec	1.1968	0.5890	0.6910
	Taklimakan	AERONET	0.1597	0.4932	0.4531
		Fennec	1.1480	0.6659	0.6891
South Africa	Namib-1	AERONET	0.0943	0.6839	0.4663
		Fennec	0.9541	0.8274	0.6973
	Namib-2	AERONET	0.1252	0.5603	0.4604
		Fennec	1.0469	0.7303	0.6961
North America	Arizona	AERONET	0.1609	0.5480	0.4524
		Fennec	1.1923	0.6975	0.6781
	Atacama	AERONET	0.1239	0.6213	0.4601
South America	Patagonia	Fennec	1.0824	0.7687	0.6855
		AERONET	0.2050	0.4666	0.4432
	Patagonia	Fennec	1.2840	0.6196	0.6743
Australia	Australia	AERONET	0.2392	0.3750	0.4348
		Fennec	1.2947	0.5390	0.6808

(i.e., BT_{dust} minus BT_{clean} (see Table 4) with different combination of SSA from 0 and 1.0 and g-factor from 0 to 1.0. The dBT result is shown as the color contour in Fig. 8a. When SSA approaches zero, the scattering effect of dust diminishes, which explains the independence of dBT on the g-factor, and in this case, the dust layer can be regarded as a purely absorbing gas layer. Because the dust layer is much colder than the surface, its absorption effect dominates, leading to a negative dBT around -2 K. When SSA attains to unity and g-factor approaches zero (i.e., lower right corner of Fig. 8a), the backward scattering effect dominates, and the emission of thermal infrared radiation by the dust layer diminishes. This condition yields the most negative dBT. When both SSA and g-factor approach unity (i.e., upper right corner of Fig. 8a), the scattering occurs largely in forward direction and the emission from the surface can “pass” through the dust layer despite the strong scattering. In this condition, the dust layer is apparently “transparent” leading to zero dBT.

After understanding how dBT varies with hypothetical SSA and g-factor in this case, we over-plot the “real” SSA and g-factor computed based on a different combination of dust PSDs and RIs (i.e., color lines with dot marker). Each of the eight color lines corresponds to one of the eight RI in the Sahara and Sahel deserts (see Fig. 4) in the Di-Biagio database. Each dot marker in a line corresponds to a lognormal dust PSD with an effective radius (r_e) from $0.4 \mu\text{m}$ to $7.7 \mu\text{m}$ with one standard deviation of $0.6 \mu\text{m}$. Furthermore, we use the black stars to indicate the scattering properties based on the AERONET PSD and blue stars for the Fennec PSD. When dust size is small, both SSA and g-factor are close to zero. As dust size increases, the SSA first increases faster than the g-

factor. But after passing about the size of AERONET PSD, the SSA remains almost invariant for a given RI while the g-factor keeps increasing. For a given dust size, the variation of RI mainly affects the SSA and has little influence on the g-factor, which is consistent with the discussion in Fig. 5. Combining the behavior of line plots and background color contour, one can see that the dBT simulation at $10.6 \mu\text{m}$ is more sensitive to dust PSD than RI. It also becomes clear that with the same $DAOD_{\text{TIR}}$ input, the BT_{dust} simulated based on the Fennec PSD is warmer than that on the AERONET PSD due to the contrast in g-factor. In other words, when retrieving $DAOD_{\text{TIR}}$ from the same observed dBT, the retrieved $DAOD_{\text{TIR}}$ based on the Fennec PSD is larger than that based on AERONET PSD, as shown in Fig. 7d.

In the second case, a dust layer extends from about 6.0 km to 0.5 km but concentrates mostly near the surface. Moreover, there is a temperature inversion (TI) in the upper boundary layer between 0.5 km and 1.25 km. Such TI was often observed over the coastal region near the Sahara Desert. It is believed to be the result of the warmer Saharan Air Layer overlaying colder Atlantic Ocean surface (Dunin and Velden, 2004; Gutleben et al., 2019; Wong et al., 2009). Both the lower altitude and the temperature inversion help enhance the emission effect of dust. As a result, the dependence of dBT on SSA and g-factor in the case (see Fig. 8d) is quite different from that in the first case (Fig. 8a). In particular, the dependence of dBT on the SSA and, therefore, the choice of RI is significantly stronger due to a more substantial emission effect. It implies that using a pre-assumed RI for $DAOD_{\text{TIR}}$ retrieval when the real RI has significant variability could induce larger uncertainty when the dust emission is strong. Fortunately, as discussed later in Section 5, TI is mainly found in the narrow coastal regions of North Africa and the Middle East (Clarisse et al., 2019).

Generally, for the transported dust with the sub-tropical atmospheric states (Fig. 8a), the assumed dust PSD dominates the $DAOD_{\text{TIR}}$ retrieval uncertainty due to the a priori dust assumption. The uncertainty due to dust RI assumption should be noticed if the dust emission effect is enhanced by TI, which would occur over the coastal region near dust sources.

3.6. Uncertainty analysis and post-screening

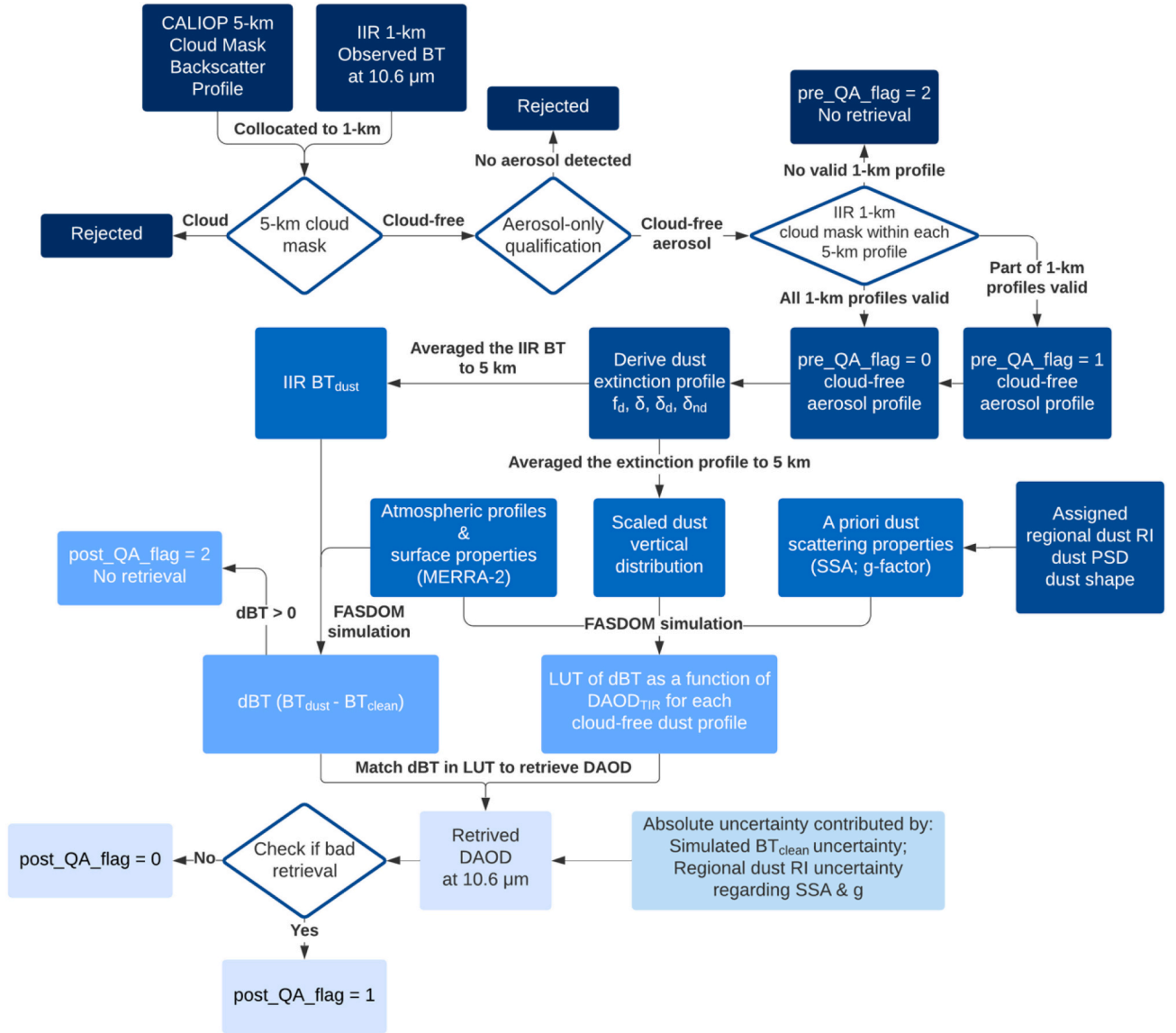
As we separate $DAOD_{\text{TIR}}$ retrieval into two sets based on two dust PSDs, the difference between the two retrievals is served as the estimation of uncertainty due to dust size. Apart from this, the uncertainty from observation, atmospheric assumption and a priori dust RI is further quantified for the global retrieval results.

As mentioned in Section 2.2, the BT_{clean} difference with a standard deviation, S_{dBT} , can be counted as the combined uncertainty in the instrument, ancillary data (e.g., MERRA-2 profiles), and radiative transfer simulation. For nighttime observations of the IIR $10.6 \mu\text{m}$ channel over ocean, we use $S_{\text{dBT}}=0.856$ K (as shown in Fig. 2b). The influence of the uncertainty in dust RI is decomposed into two parts corresponding to the impacts of dust RI on SSA and g-factor, respectively. Based on these considerations, we propose to use the following equation to estimate the uncertainty in the retrieved DAOD:

$$s_{\text{DAOD}} = \sqrt{\left(\frac{\partial \text{DAOD}}{\partial \text{dBT}}\right)^2 s_{\text{dBT}}^2 + \left(\frac{\partial \text{DAOD}}{\partial \text{SSA}}\right)^2 s_{\text{SSA}}^2 + \left(\frac{\partial \text{DAOD}}{\partial g}\right)^2 s_g^2} \quad (2)$$

where s_{DAOD} is the absolute uncertainty on the retrieved DAOD, s_{SSA} and s_g are the standard deviation of SSA and g-factor, respectively, which are calculated based on each regional RIs in the corresponding RI regime. The perturbation of dBT is 20% of the observed IIR dBT (i.e., IIR $BT_{\text{cdust}} - \text{FASDOM } BT_{\text{clean}}$), while the perturbations of SSA and g-factor are the difference between the maximum and minimum values calculated from the regional RIs. The corresponding change of DAOD to the perturbation is then used to obtain $\frac{\partial \text{DAOD}}{\partial \text{dBT}}$, $\frac{\partial \text{DAOD}}{\partial \text{SSA}}$ and $\frac{\partial \text{DAOD}}{\partial g}$.

To evaluate the retrieval uncertainty, we implement the retrieval on

Fig. 6. Flowchart of the IIR-CALIOP DAOD_{TIR} retrieval algorithm.

the IIR and CALIOP data from 2013 to 2014 based on Fennec PSD after applying $\text{pre_QA} \leq 1$. Fig. 9a shows the histogram of the three propagation terms of uncertainties in Eq. (2) for the two-year data. As explained earlier in Section 3.5, dust RI contributes only ~10% of the DAOD uncertainty by the perturbation on SSA and g-factor. About 90% of the uncertainty comes from the term of dBT uncertainty, representing the uncertainty from instrumental noise, atmospheric assumptions, and radiative simulations. Fig. 9b shows the averaged relative retrieval uncertainty of DAOD_{10.6μm}. For samples with relatively small DAOD_{10.6μm} (< 0.1), the relative retrieval uncertainty rapidly exceeds 100% mainly due to the low signal-to-noise ratio. Based on these observations, we propose to utilize the collocated CALIOP DAOD_{532nm} as one of the factors to control the quality of the retrieval for the samples with relatively low DAOD.

Based on Fig. 5b and previous studies (Song et al., 2018), the ratio of DAOD_{10.6μm} to DAOD_{532nm} is most likely smaller than unity. Including the mean retrieval uncertainty indicated in Fig. 9b, retrievals are expected to get close to or exceed 100% relative uncertainty. As a result, we consider the retrieval to be no longer physically meaningful if the ratio of DAOD_{10.6μm} to DAOD_{532nm} is greater than 2. Fig. 9c shows the histogram of CALIOP DAOD_{532nm} by separating the samples to two

categories, with the ratio of DAOD_{10.6μm} to DAOD_{532nm} less than 2 and greater than 2, respectively. We find that the retrievals with the ratio greater than 2 are dominant when CALIOP DAOD_{532nm} is smaller than 0.05. Therefore, we conclude that the DAOD_{10.6μm} retrieval is too noisy for the samples with CALIOP DAOD_{532nm} < 0.05 . Instead, we simply set their DAOD_{10.6μm} as $\text{DAOD}_{532nm} \cdot Q_{\text{ext}, 10.6\mu\text{m}} / Q_{\text{ext}, 532nm}$, where $Q_{\text{ext}, 10.6\mu\text{m}} / Q_{\text{ext}, 532nm}$ is introduced in Section 3.3 as TIR/VIS ratio as shown in Fig. 5b and Table 3.

For retrievals with CALIOP DAOD_{532nm} ≥ 0.05 , there are still a small fraction of non-retrieval-attempted cases (1.72%) with the simulated BT_{dust} warmer than BT_{clean}. Although it is theoretically possible if a significant temperature contrast between the dust layer and the surface occurs, it also requires a strong dust absorption effect, which is hardly achieved by the a priori dust at the 10.6 μm channel (see Fig. 8d). Therefore, we believe that these cases are due to the uncertainty in the observation and/or radiative transfer simulation and are set to be with “post_QA = 2” as shown in Table 2.

Fig. 10a and b show the global distribution of the mean DAOD_{10.6μm} and mean uncertainty for two-year data from 2013 to 2014 after applying “pre_QA ≤ 1 ” and “post-QA ≤ 1 ”, which excludes the two types of non-retrieval-attempted samples with “pre_QA = 2” and “post-QA =

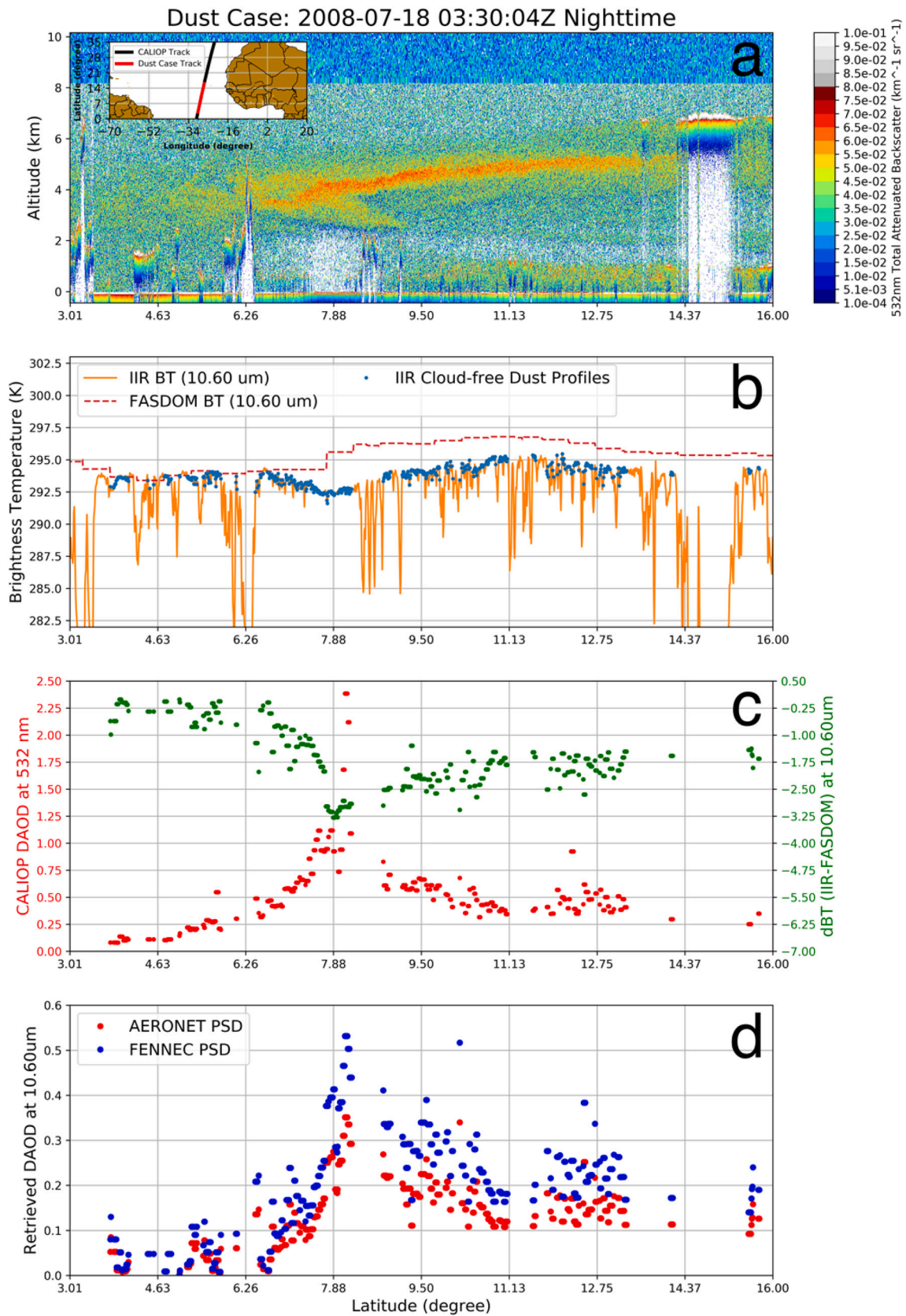


Fig. 7. (a) The CALIOP total attenuated backscatter at 532 nm on July 18th, 2008, in Tropical North Atlantic (the orbit at upper left). (b) The IIR BT_{dust} at 10.6 μm (orange lines) and the FASDOM BT_{clean} at 10.6 μm (red dash lines), respectively. (c) The CALIOP DAOD (red dots) of cloud-free dust-laden profiles and the dBT (IIR-FASDOM) (green dots) are corresponding to the left and right y-axis, respectively. (d) The retrieved DAOD_{10.6 μm} using Fennec PSD (blue lines) and AERONET PSD (red lines). (For interpretation of the references to color in this figure legend, the reader is referred to the web version of this article.)

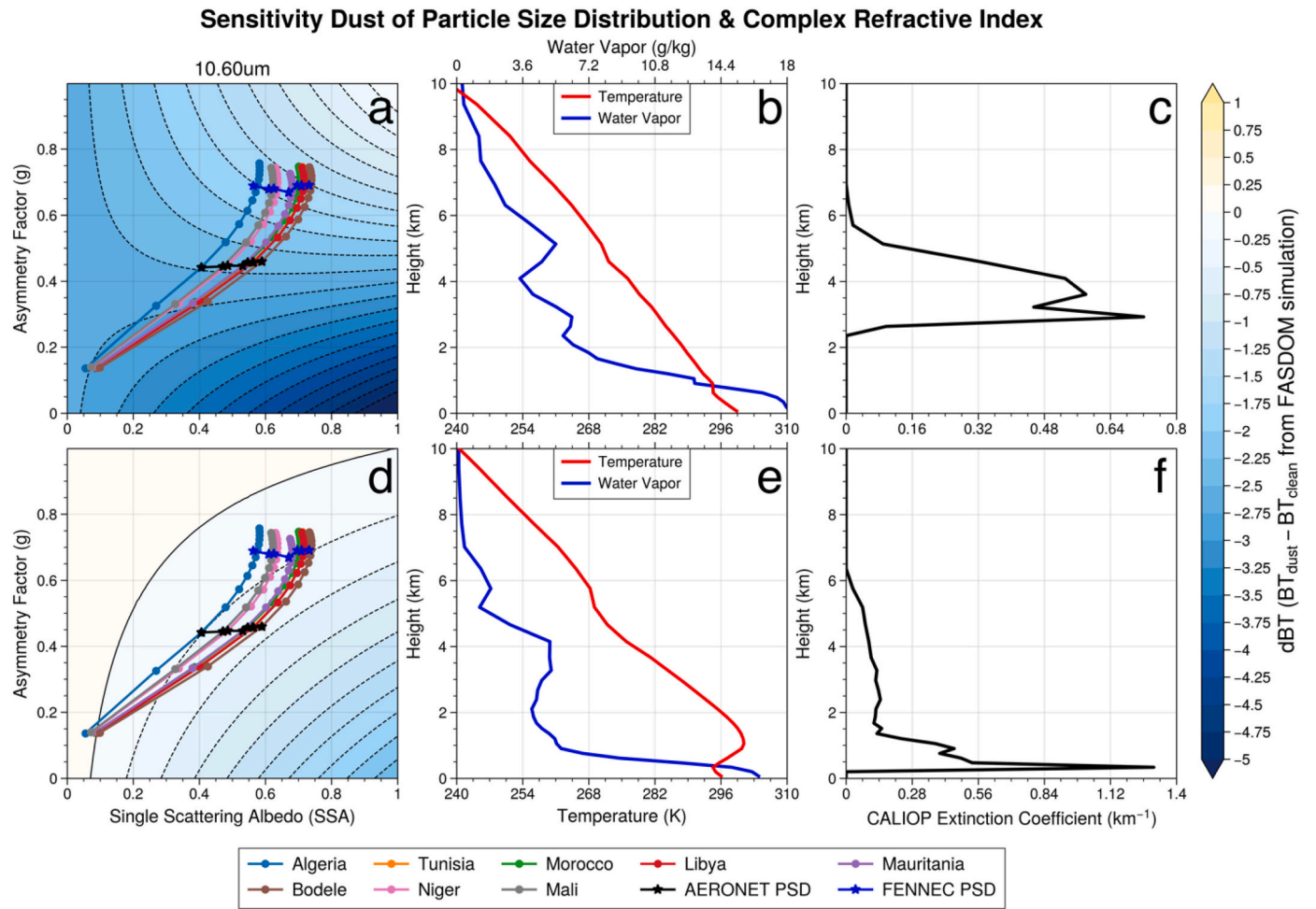


Fig. 8. (a) and (d) represent the contours of dBT between BT_{clean} and BT_{dust} from the FASDOM simulation at IIR Band $10.6 \mu m$ with perturbed g factor (y-axis) and SSA (x-axis) by the given $DAOD_{TIR}$ (value of 0.2) corresponding to the sub-tropical (b) and SAL (e) atmospheric profiles, respectively. (c) and (f) represent the corresponding vertical profiles of dust extinction coefficient with the atmospheric profiles of (b) and (e), respectively. The real and dash contour lines represent positive and negative values of dBT, respectively. The dot lines with color in (a) and (d) represent the g -factor and SSA calculated based on combinations of Di-Biagio RIs in Sahara/Sahel deserts and the perturbed PSDs. Each dot marker in a line corresponds to a lognormal dust PSD with an effective radius (r_e) from $0.4 \mu m$ to $7.7 \mu m$ with one standard deviation of $0.6 \mu m$. Stars with solid lines in (a) and (d) represent the g -factor and SSA based on AERONET PSD (black) and Fennec PSD (blue) with corresponding dust RIs.

Table 4

Parameters in the sensitivity study for the selected cases.

Time	Geolocation	Surface temperature	Surface emissivity at $10.6 \mu m$	Integrated water vapor path	Simulated BT_{clean}	Input $DAOD_{TIR}$
2008-07-18 03:30:04 UTC	7.5°N, 28.75°W	301.462 K	0.984	5.510 g/cm ²	295.612 K	0.2
2006-07-01 03:03:34 UTC	16.5°N, 20.625°W	296.672 K	0.984	2.722 g/cm ²	294.853 K	0.2

2". Note that there are unreliaibly high $DAOD_{10.6\mu m}$ over the Southern Ocean between the 30°S and 60°S and Northwestern Atlantic above 35°N in Fig. 10a. As the synergic CALIOP $DAOD_{532nm}$ is useful for identifying unconfident retrieval results, we assign "post_QA = 0" for results with a ratio $DAOD_{10.6\mu m} / DAOD_{532nm} < 2$ and "post_QA = 1" for results with a ratio $DAOD_{10.6\mu m} / DAOD_{532nm} \geq 2$. Fig. 10b and d show the mean $DAOD_{10.6\mu m}$ and mean uncertainty after imposing the "post_QA = 0" to the results in Fig. 10a and c. As the retrievals with "post_QA = 1" are excluded, the retrievals with suspiciously large $DAOD$ value over the Southern Ocean are mostly removed. In the rest of the paper, the retrieval results are all applied QA flags with "pre_QA ≤ 1 " and "post_QA = 0".

4. Retrieval results

4.1. Spatial and temporal pattern of $DAOD$ at $10.6\mu m$

In this section, we present the climatological $DAOD_{10.6\mu m}$ retrieval results from 2013 to 2019 from our algorithm as explained above. Fig. 11 shows the seasonal variation of the retrieved $DAOD_{10.6\mu m}$ based on the AERONET PSDs (left column, referred to as "AERONET $DAOD_{10.6\mu m}$ " hereafter) and Fennec PSD (middle column, hereafter "Fennec $DAOD_{10.6\mu m}$ "). We also plot the CALIOP $DAOD_{532nm}$ based on the method in Section 3.2 (right column) for comparison purposes. As the retrieval uncertainties of $DAOD_{532nm}$ are not evaluated in this study, instead of focusing on the absolute value of $DAOD_{532nm}$, we use the

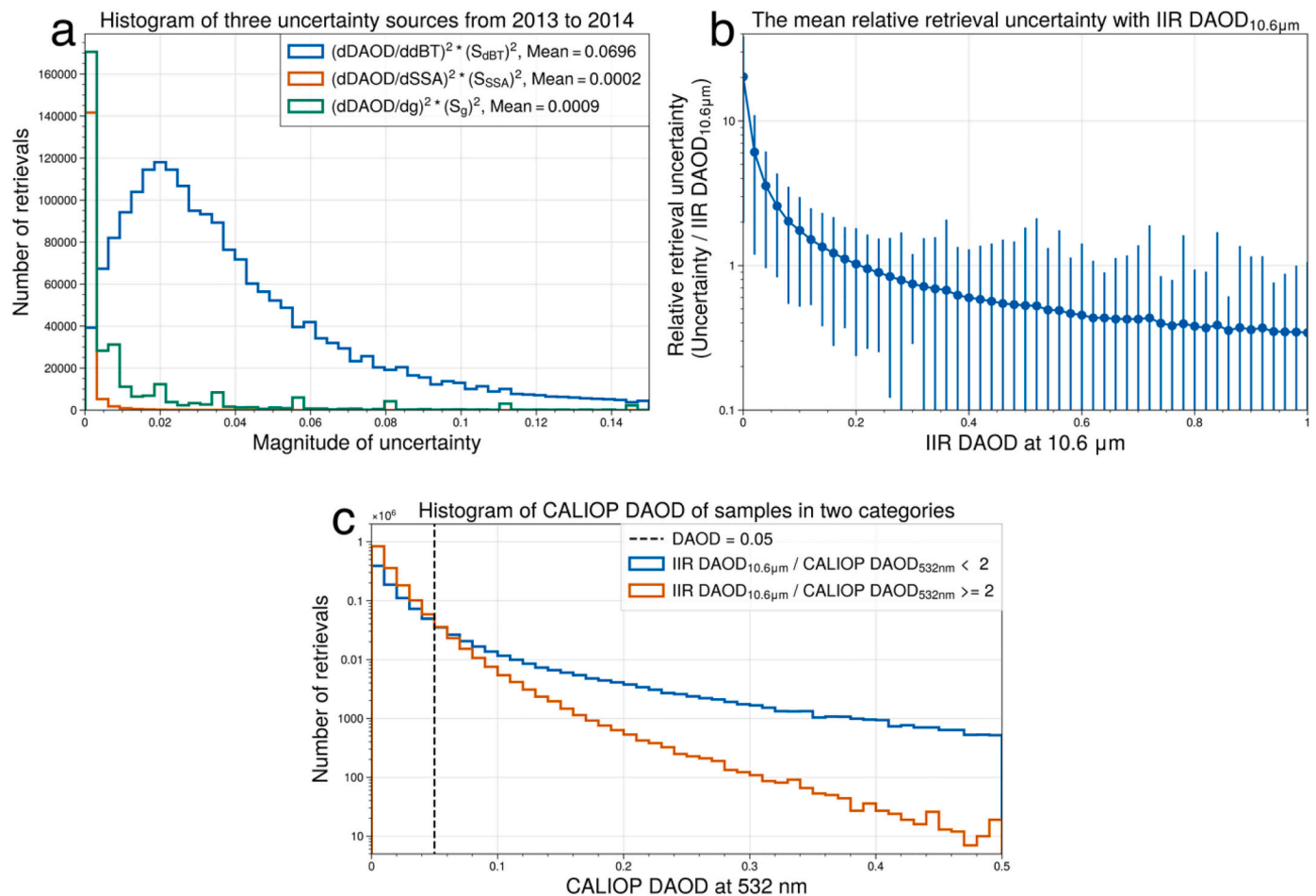


Fig. 9. (a) The histogram of three uncertainty propagations ($(\frac{\partial DAOD}{\partial BT})^2 S_{dBt}^2$, $(\frac{\partial DAOD}{\partial SSA})^2 S_{SSA}^2$ and $(\frac{\partial DAOD}{\partial g})^2 S_g^2$) for retrievals from 2013 to 2014. (b) The mean relative retrieval uncertainty (i.e., $S_{DAOD}/DAOD_{10.6\mu m}$) varied with $DAOD_{10.6\mu m}$. The y-axis is on a logarithmic scale. (c) The histogram of CALIOP $DAOD_{532nm}$ of two categories, one is the samples with $DAOD_{532nm}/DAOD_{10.6\mu m} < 2$ (blue) and the other is the samples with $DAOD_{532nm}/DAOD_{10.6\mu m} \geq 2$ (red). The black dash line indicates the CALIOP $DAOD_{532nm}$ with value of 0.05. The y-axis is on a logarithmic scale. (For interpretation of the references to color in this figure legend, the reader is referred to the web version of this article.)

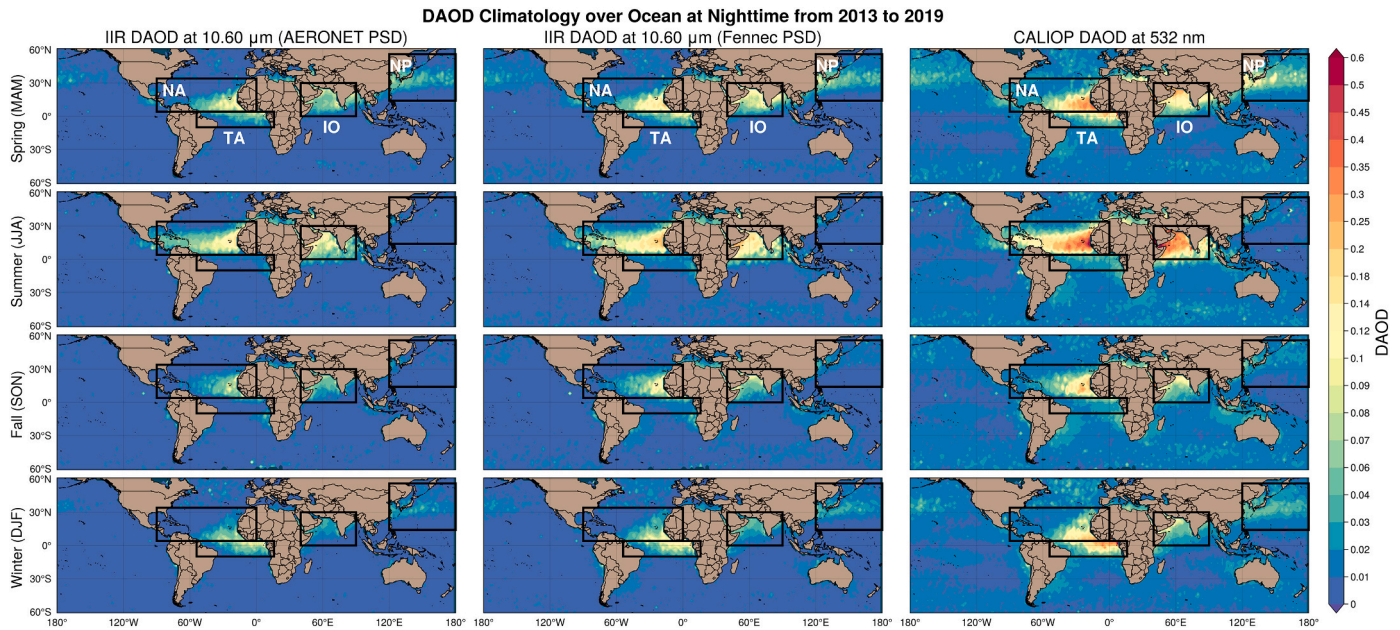
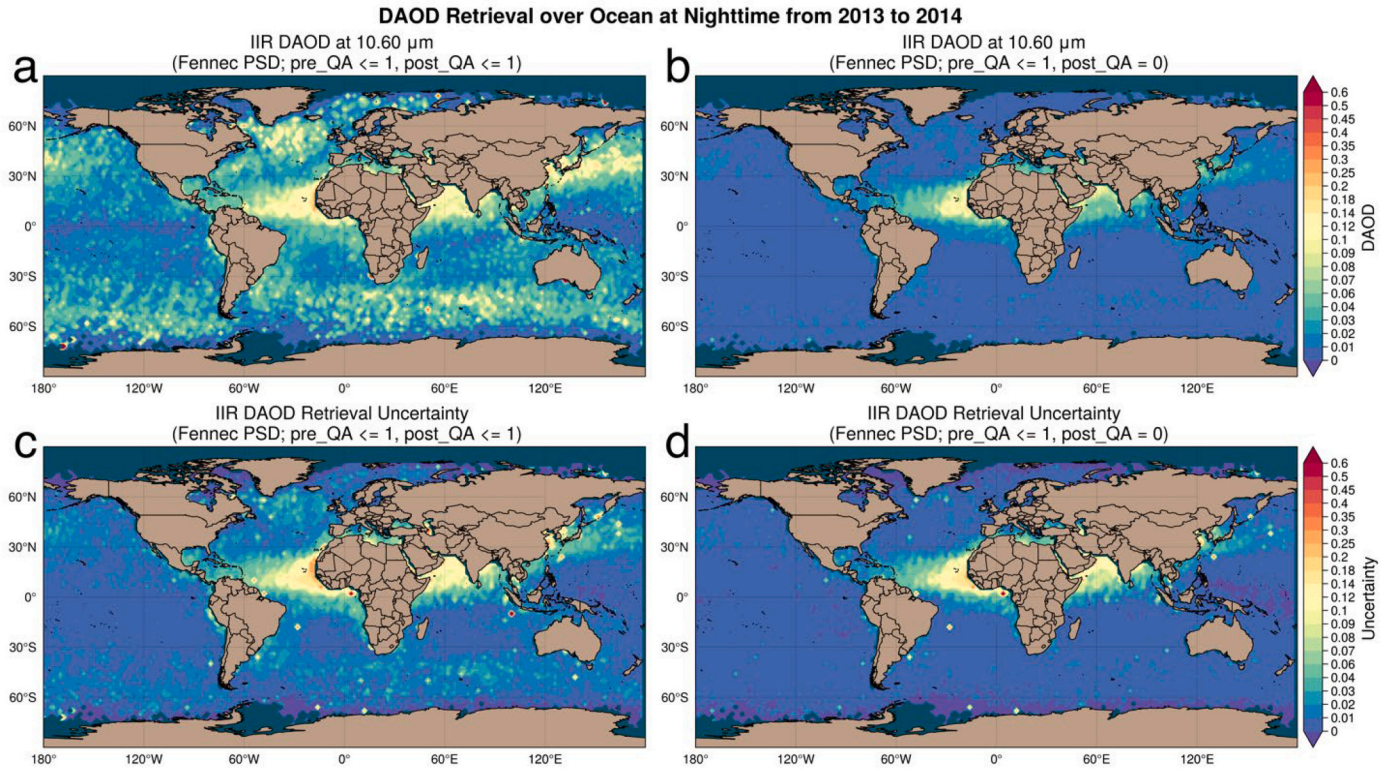
$DAOD_{532nm}$ as the reference for the seasonal variation patterns of the retrieved $DAOD_{10.6\mu m}$ and the implication of the ratio between VIS (i.e., 532 nm) and TIR (i.e., 10.6 μm). Table 5 shows the seasonal-averaged DAOD retrieved from IIR and CALIOP using AERONET and Fennec PSD, and from IASI observation based on two different methods developed by Capelle et al., 2018 and Clarisse et al., 2019. Note that the global average weighted by surface areas excludes the polar region where dust is rarely found. The relatively larger annual global mean Fennec $DAOD_{10.6\mu m}$ (0.013 in Table 5) compared with that of AERONET $DAOD_{10.6\mu m}$ (0.008 in Table 5) reflects the retrieved $DAOD_{TIR}$ uncertainty due to dust PSD assumptions, which is discussed in Section 3.5. We also highlight regional mean DAODs over four active dust transport regions (i.e., North Atlantic (NA), Tropical Atlantic (TA), Indian Ocean (IO) and Northwest Pacific (NP)) with geolocation range in Fig. 11 and Table 5. The detailed comparisons of the retrieval with the two IASI products are discussed in Section 4.2.

In spring, the outflow of Asian dust over NP is seen from CALIOP $DAOD_{532nm}$ as well as both retrieved $DAOD_{10.6\mu m}$. However, the $DAOD_{10.6\mu m}$ decreases faster eastward of 180°W than the $DAOD_{532nm}$. It indicates that the coarse dust particles deposit to the ocean during transport, leading to a reduction of both dust size and total AOD, and therefore a reduced signal for the TIR retrieval. In summer, the $DAOD_{10.6\mu m}$ captures the outbreaks of dust transport from Sahara and Sahel to NA, with averaged values ranging from 0.04 to 0.06. Meantime, dust with an average DAOD from 0.08 to 0.12 over IO is mainly

transported from the regional source regions (e.g., the Thar Desert) and the source regions over the Middle East and North Africa (Banerjee et al., 2019). In autumn, the dust transport over NA, IO, and NP is weakened compared to summer. In winter, the south-shifted trade wind in the northern hemisphere drives more dust transport to TA than NA. We find the highest $DAOD_{532nm}$ (~0.1) and $DAOD_{10.6\mu m}$ (0.03–0.05) over TA in winter compared with other seasons. Meanwhile, dust has more chance to mix with smoke and biomass burning aerosols emitted from Tropical Africa. The mean $DAOD_{532nm}$ in winter over TA shares a similar average value (~0.1) with that in summer over NA, while the mean $DAOD_{10.6\mu m}$ in winter over TA is lower than that (0.04–0.06) in summer over NA, implying a reduced TIR signal due to the lower fraction of dust in the mixture during the transport to TA.

Previous studies have shown that the DAOD retrievals are very useful for dust transport studies (e.g., Liu et al., 2008; Huang et al., 2008; Yu et al., 2008). In Fig. 12, we present the seasonal meridional mean of the two $DAOD_{10.6\mu m}$ and CALIOP $DAOD_{532nm}$ over NA and NP in their dust outbreak seasons (i.e., summer over NA and spring over NP) from 2013 to 2019. A clear westward and eastward decreasing trend of DAOD is observed in the NA and NP, respectively. This is consistent with those reported in the previous studies (e.g., Huang et al., 2008; Liu et al., 2008; Yu et al., 2019; Yu et al., 2015a). A detailed study of the long-range transport of dust is however beyond the scope of this study and will be left for the future.

As mentioned in Section 3.5, the assumption of dust PSD impacts the



$DAOD_{TIR}$ retrieval, which is presented by the difference between AERONET and Fennec $DAOD_{10.6\mu m}$ in Table 5 and Figs. 11 and 12. However, without the TIR observation, to obtain $DAOD_{TIR}$, we must extend the CALIOP $DAOD_{532nm}$ to the TIR region. How would the extended results be compared to the retrieved $DAOD_{10.6\mu m}$? With this question, we

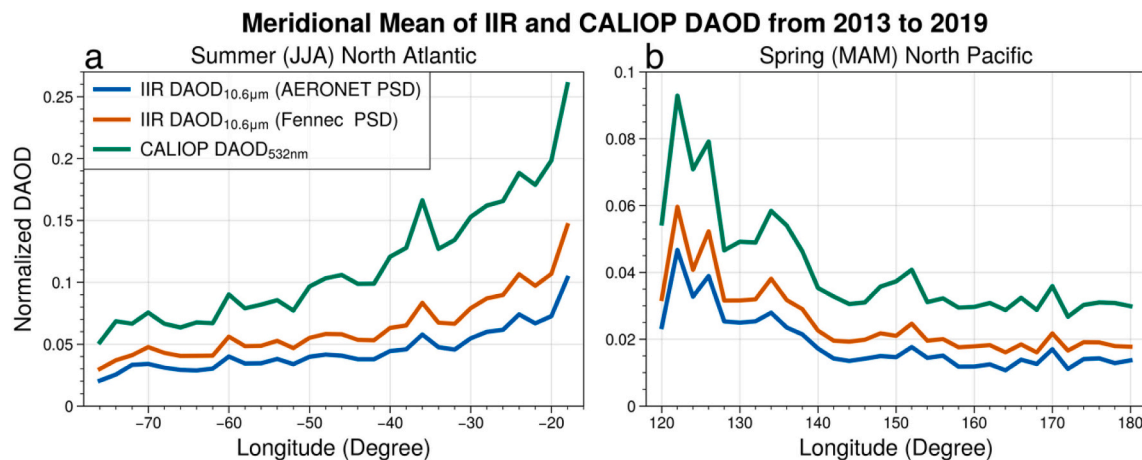
performed the following investigations.

First, we convert the 7-year averaged CALIOP $DAOD_{532nm}$ in summer to be $DAOD$ at $10.6\mu m$ based on the equation $DAOD_{10.6\mu m} = DAOD_{532nm} \cdot Q_{ext, 10.6\mu m} / Q_{ext, 532nm}$, where the $Q_{ext, 10.6\mu m} / Q_{ext, 532nm}$ is introduced in Section 3.3 as TIR/VIS ratio (referred to as “CALIOP-converted

Table 5

The seasonal and global/regional mean of all retrieved DAOD from 2013 to 2019.

Product	Season	Global (60°S ~ 60°N)	Regions			
			North Atlantic (4°N ~ 34°N, 90°W ~ 0°)	Tropical Atlantic (10°S ~ 4°N, 54°W ~ 14°E)	Indian Ocean (0° ~ 30°N, 40°E ~ 70°E)	Northwest Pacific (14° ~ 56°N, 120°E ~ 180°)
IIR AERONET DAOD _{10.6μm}	Spring	0.008	0.026	0.029	0.049	0.017
	Summer	0.010	0.042	0.010	0.080	0.003
	Autumn	0.006	0.017	0.009	0.035	0.005
	Winter	0.006	0.015	0.036	0.020	0.010
	Annual	0.008	0.025	0.021	0.046	0.009
IIR Fennec DAOD _{10.6μm}	Spring	0.014	0.037	0.039	0.070	0.023
	Summer	0.016	0.060	0.017	0.118	0.006
	Autumn	0.011	0.027	0.015	0.049	0.009
	Winter	0.010	0.022	0.050	0.029	0.015
	Annual	0.013	0.036	0.031	0.066	0.013
CALIOP DAOD _{532nm}	Spring	0.026	0.066	0.073	0.128	0.038
	Summer	0.030	0.105	0.029	0.251	0.012
	Autumn	0.020	0.044	0.027	0.078	0.017
	Winter	0.020	0.044	0.100	0.055	0.024
	Annual	0.024	0.065	0.057	0.128	0.023
IASI-ULB DAOD _{10.0μm}	Spring	0.003	0.020	0.018	0.035	0.012
	Summer	0.003	0.044	-0.001	0.070	-0.004
	Autumn	-0.002	0.008	-0.007	0.011	-0.008
	Winter	-0.001	0.005	0.019	0.004	-0.001
	Annual	0.001	0.019	0.007	0.030	-0.001
IASI-LMD DAOD _{10.0μm}	Spring	0.027	0.048	0.047	0.080	0.022
	Summer	0.032	0.096	0.019	0.185	0.028
	Autumn	0.021	0.040	0.016	0.041	0.017
	Winter	0.024	0.027	0.043	0.029	0.013
	Annual	0.026	0.053	0.031	0.084	0.020

**Fig. 12.** The meridional mean climatological CALIOP DAOD_{532nm} (green), AERONET DAOD_{10.6μm} (blue) and Fennec DAOD_{10.6μm} (red) over the North Atlantic in summer (a) and North Pacific in spring (b) from 2013 to 2019. (For interpretation of the references to color in this figure legend, the reader is referred to the web version of this article.)

DAOD_{10.6μm}”). As shown in Fig. 5b, Fennec PSDs’ TIR/VIS ratio is from 0.35 to 0.5 at 10.6 μm, which can be 4 to 6 times larger than that of AERONET PSD (from 0.05 to 0.14). Consequently, the CALIOP-converted DAOD_{10.6μm} based on AERONET PSD is substantially smaller than that based on Fennec PSD (see Fig. 13a and c), leading to a significant difference (~0.125) between the two CALIOP-converted DAOD_{10.6μm} as shown in Fig. 13e. Next, we retrieve the corresponding 7-year averaged AERONET DAOD_{10.6μm} and Fennec DAOD_{10.6μm} as shown in Fig. 13b and d.

In Fig. 13e and f, the difference of IIR-retrieved DAOD_{10.6μm} due to the change of dust PSD is remarkably reduced by ~70% compared with converted CALIOP-converted DAOD_{10.6μm}. The possible reason is discussed as follows. Firstly, the CALIOP-converted DAOD_{10.6μm} linearly depends on the TIR/VIS ratio, which is highly varied with dust PSD as shown in Fig. 5 and previous studies (Fig. 7 in Song et al., 2018). Secondly, as the observed dBT provides information on dust extinction,

including absorption and scattering, changing the dust PSD assumption varies the dust SSA and g-factor in the retrieval. With the unchanged dust RI, the dependency of g-factor on dust PSD eventually determines dBT and hence the IIR-retrieved DAOD_{10.6μm}, as discussed in Section 3.5 (see Fig. 8a and d). Therefore, with the TIR observation, the change of TIR/VIS ratio by dust PSD no longer has an impact on DAOD_{10.6μm}. Instead, the change of dust scattering properties, in this case, the g-factor, by dust PSD determines the difference in the IIR-retrieved DAOD_{10.6μm} (see Fig. 13f). The moderate variation of dBT based on the change of dust PSD in the retrieval could be the reason leading to a less varied retrieved DAOD_{10.6μm} than the converted DAOD_{10.6μm}. However, we should keep in mind that this result is neither guaranteed in using other TIR wavelengths nor in other combinations of a priori dust assumptions. A more dedicated study is needed for future research.

There is another interesting point to note in Fig. 13. By comparing the CALIOP-converted DAOD_{10.6μm} with the IIR-retrieved DAOD_{10.6μm}

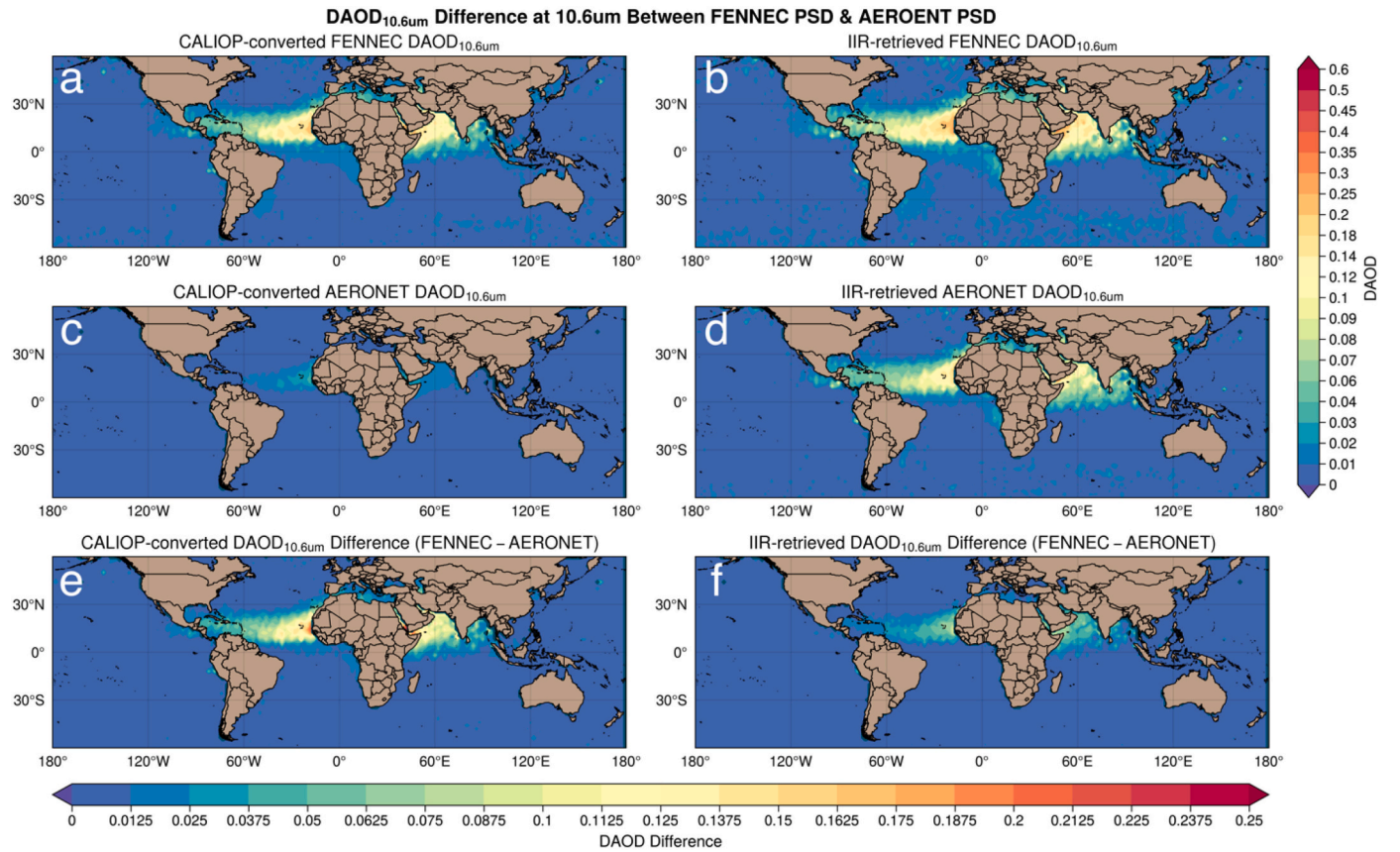


Fig. 13. The global distribution of a) the mean CALIOP-converted DAOD_{10.6 μm} based on Fennec PSD and c) AERONET PSD, and b) the mean IIR-retrieved DAOD_{10.6 μm} based on Fennec PSD and d) AERONET PSD, in summer (JJA) of 7-years IIR-CALIOP observation from 2013 to 2019. e) The difference of the CALIOP-converted DAOD_{10.6 μm} between two PSD assumptions. f) The difference of the mean IIR-retrieved DAOD_{10.6 μm} between two PSD assumptions.

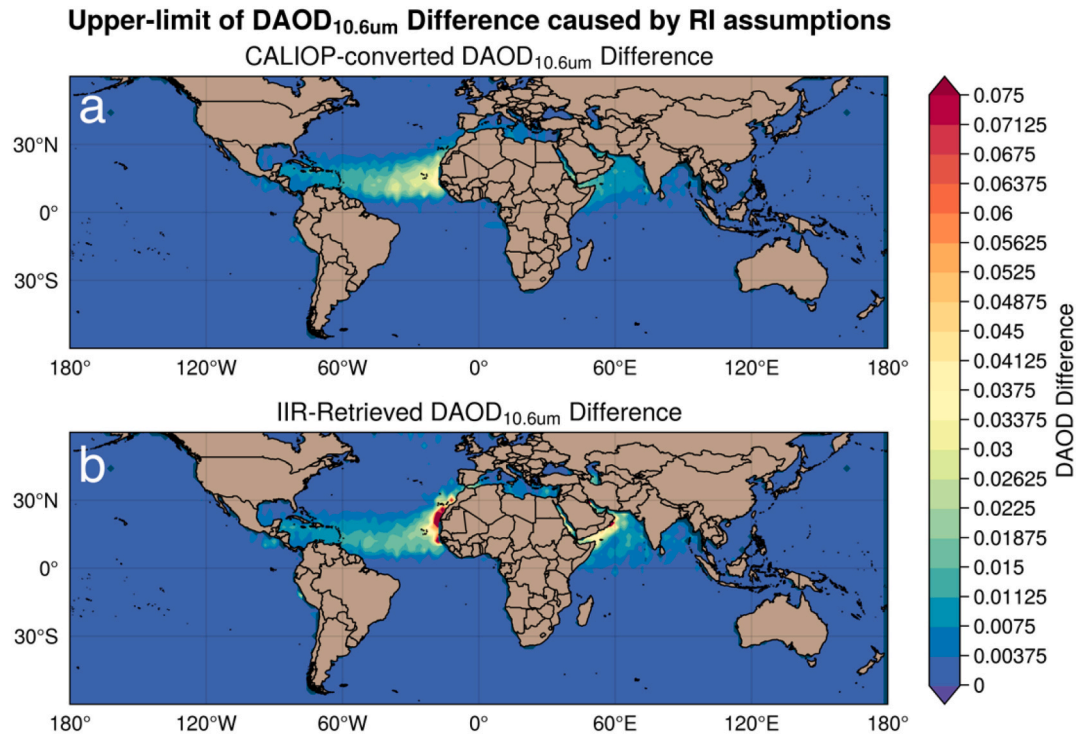


Fig. 14. The global distribution of the upper-limit DAOD difference of a) the mean CALIOP-converted DAOD_{10.6μm} and b) the mean IIR-retrieved DAOD_{10.6μm} in summer (JJA) of 7-years IIR-CALIOP observation from 2013 to 2019. The dust PSD assumption is fixed to be Fennec PSD.

based on the same dust PSD in Fig. 13, we found that the consistency between the CALIOP-converted $\text{DAOD}_{10.6\mu\text{m}}$ and the IIR-retrieved $\text{DAOD}_{10.6\mu\text{m}}$ based on the Fennec PSD is better than that based on the AERONET PSD. This accordance means using the Fennec PSD is more suitable for representing the dust extinction spectrum in both VIS and TIR as Song et al. (2018) suggested at the point of view in dust DRE. It opens an exciting perspective for utilizing the synergic VIS and TIR observation to constraint the DAOD_{TIR} , the dust PSD and further the global dust cycle and DRE_{LW} simulation (Song et al., 2018; Wu et al., 2020).

Following the similar procedure as in Fig. 13, we also investigate the sensitivity of CALIOP-converted and IIR-retrieved $\text{DAOD}_{10.6\mu\text{m}}$ to dust RI. Note that in this investigation we keep the dust PSD fixed as Fennec. Firstly, we calculate the maximum and minimum CALIOP-converted $\text{DAOD}_{10.6\mu\text{m}}$ based on the maximum and minimum TIR/VIS ratios from each of the seven assigned RI regimes. The difference between the maximum and minimum CALIOP-converted $\text{DAOD}_{10.6\mu\text{m}}$ (see Fig. 14a) represents the upper-limit uncertainty of CALIOP-converted $\text{DAOD}_{10.6\mu\text{m}}$ caused by dust RI assumptions. Afterward, according to different RI regimes, we retrieve the DAOD based on all the assigned regional RIs. The maximum and minimum IIR-retrieved $\text{DAOD}_{10.6\mu\text{m}}$ in each RI regime are used to quantify the upper-limit uncertainty of IIR-retrieved $\text{DAOD}_{10.6\mu\text{m}}$ contributed from dust RI assumptions (see Fig. 14b). Comparing Fig. 14a with Fig. 14b, except the coastal regions of West Africa and Arabian Peninsula, the global averaged difference of retrieved $\text{DAOD}_{10.6\mu\text{m}}$ caused by RI assumptions is $\sim 26\%$ smaller than that of CALIOP-converted $\text{DAOD}_{10.6\mu\text{m}}$ caused by RI assumptions. Once again, this result indicates that thanks to the observational constraints, the IIR-retrieved $\text{DAOD}_{10.6\mu\text{m}}$ is less susceptible to the uncertainty in RI assumptions than CALIOP-converted results.

Although the comparison of CALIOP-converted $\text{DAOD}_{10.6\mu\text{m}}$ and retrieved $\text{DAOD}_{10.6\mu\text{m}}$ based on the two different dust PSDs are discussed in summer for the 7-year averaged data, the DAOD differences are not impacted by the seasonal variation of DAOD. It is because the TIR/VIS ratio used for the CALIOP-converted $\text{DAOD}_{10.6\mu\text{m}}$ and the SSA and g-factor used for the retrieved $\text{DAOD}_{10.6\mu\text{m}}$ are independent with seasonal variations. Therefore, the results discussed above are also applicable for other seasons.

4.2. Comparison with IASI-retrieved DAOD

As suggested in the previous section, the Fennec $\text{DAOD}_{10.6\mu\text{m}}$ makes a better agreement with the theoretically CALIOP-converted $\text{DAOD}_{10.6\mu\text{m}}$. Therefore, to evaluate the IIR-CALIOP retrieval, we compare the Fennec $\text{DAOD}_{10.6\mu\text{m}}$ with two independent IASI-based DAOD at $10\mu\text{m}$ ($\text{DAOD}_{10\mu\text{m}}$) products developed by different teams. The first one is derived by the group at Laboratoire de Météorologie Dynamique (LMD) (referred to as “IASI-LMD”) and the other by the group at Université libre de Bruxelles (ULB) (referred to as “IASI-ULB”). The IASI-LMD algorithm has a long history. It was initiated by Pierangelo et al. (2004) for AIRS and further developed as a decadal dataset for IASI by several follow-up studies (Capelle et al., 2018; Capelle et al., 2014; Peyridieu et al., 2013). It uses a LUT-based retrieval method to retrieve both DAOD at $10\mu\text{m}$ and the mean dust layer altitude based on the selected channels of IASI. Instead of using LUTs, the IASI-ULB algorithm utilizes an artificial neural network (NN) method to learn the dust spectral characteristics represented by the dust index R based on the observed outgoing longwave spectral radiance (Clarisse et al., 2019). The retrieved DAOD is then obtained by multiplying the observed R with the NN-predicted conversion ratio CR. The NN training process is based on the given atmospheric conditions, dust properties, the monthly mean CALIOP dust altitude and the given IASI observation. As the observed R contains the independent random instrumental noise with a mean of 0, it allows the retrieved DAOD to be negative for reducing bias.

The different spatiotemporal resolution between IASI and CALIPSO prevents enough reliable collocations for the pixel-by-pixel comparison.

Here, we only compare the grid-level (i.e., latitude-longitude grid) climatology between Fennec $\text{DAOD}_{10.6\mu\text{m}}$ and $\text{DAOD}_{10\mu\text{m}}$ from the IASI products. Note that the IIR-CALIOP retrieval is implemented over oceans at nighttime only, while the current IASI grid-level products include data in the daytime and over lands. To alleviate the sampling difference, we first apply the following screening procedures for the IASI level-2 (i.e., pixel-level) products in 7 years from 2013 to 2019 and then aggregate them to the corresponding grid-level climatological results ($2^\circ \times 2^\circ$ grids):

- 1) Only the nighttime samples over oceans are selected from both IASI products using their surface masks and day/night flags.
- 2) Only the filtered results after applying the required QA flags in three products are considered. For IIR/CALIOP retrieval, $\text{pre_QA} \leq 1$ and $\text{post_QA} = 0$ are applied. Quality control processes of IASI retrievals are detailed in Capelle et al. (2018) and Clarisse et al. (2019).

It is necessary to point out that both IASI products do DAOD_{TIR} retrievals on the detected cloud-free pixels with ad hoc dust detection based on the dust TIR spectral patterns. Their cloud masking and dust detection are different from those of the Lidar-based method in the IIR-CALIOP retrieval, leading to the difference in the cloud-free dust sampling. Thus, it should be carried when comparing the 7-year averaged seasonal retrieved DAOD among three products, as shown in Fig. 15. Note that there also is a spectral difference of DAOD at $10.0\mu\text{m}$ and $10.6\mu\text{m}$, which depends on the assumptions of dust PSD, RI and shape. Therefore, a perfect match of the retrieved DAOD is *not* expected in the comparison. Rather than that, all three products have a good agreement on the seasonal variations of dust transport over NP (in spring), NA and IO (in summer) and TA (in winter), with containable discrepancies of the mean DAOD value, which is listed in Table 5.

In Fig. 15, the most apparent discrepancy among $\text{DAOD}_{10.6\mu\text{m}}$ (left column), IASI-ULB and IASI-LMD $\text{DAOD}_{10\mu\text{m}}$ (middle and right columns) are over the “background” region with low DAOD (Fennec $\text{DAOD}_{10.6\mu\text{m}} < 0.01$) as the non-dust aerosol dominates. The IASI-LMD $\text{DAOD}_{10\mu\text{m}}$ over the “background” region has a significantly larger value (~ 0.06) than $\text{DAOD}_{10.6\mu\text{m}} (< 0.01)$, especially over the West Pacific “warm pool” and ITCZ, which has a high occurrence frequency of stratospheric volcanic ash and sulfur dioxide (Gupta et al., 2021; Read et al., 1993). It implies that the IASI-LMD retrieval technique might overestimate the $\text{DAOD}_{10\mu\text{m}}$ over the “background” region due to the misidentification of volcanic ash that shares a similar radiative signal in TIR as dust. (DeSouza-Machado et al., 2006; Lee et al., 2014; Taylor et al., 2015).

To better compare the retrieved DAOD grid-by-grid over the four active dust transport regions, all the grid-level seasonal mean DAODs from three retrieval products over each region are plotted in Fig. 16 with linear regression values (i.e., slope, intercept, correlation coefficient (r -value and p -value)). The comparison between $\text{DAOD}_{10.6\mu\text{m}}$ and $\text{DAOD}_{10\mu\text{m}}$ Over NA (Fig. 16a and e) and TA (Fig. 16b and f) shows well-agreed variation as the r -values are higher than 0.8. However, the corresponding slopes deviate from unity, indicating a systematic difference of the absolute value of DAOD, which is also reflected in the mean value comparison in Table 5. Over IO, in Fig. 16c and g, $\text{DAOD}_{10.6\mu\text{m}}$ is still well-agreed with IASI-ULB $\text{DAOD}_{10\mu\text{m}}$ ($r = 0.824$), while it has a lower r -value (0.770) with IASI-LMD $\text{DAOD}_{10\mu\text{m}}$. In Fig. 16d and h, dust over NP has an overall smaller DAOD (< 0.15) and would also have smaller dust particle size due to the deposition of the coarser particles during the long-term transport from Asia. As a result, the dust radiative signal is harder to be seen in TIR by IASI, leading to higher retrieval uncertainties and, therefore, the lowest r -values ($r = 0.578$ and 0.152) of $\text{DAOD}_{10.6\mu\text{m}}$ with IASI-ULB and IASI-LMD $\text{DAOD}_{10\mu\text{m}}$. However, the CALIOP DPR-based dust detection approach can better estimate them based on their non-sphericity but not on their size. Therefore, as shown in Fig. 15 for over NP in spring and winter, there is a more evident $\text{DAOD}_{10.6\mu\text{m}}$ trend of dust transport westward than both IASI $\text{DAOD}_{10\mu\text{m}}$ at around 30°N . It implies that the collocated IIR-CALIOP has a better dust detection

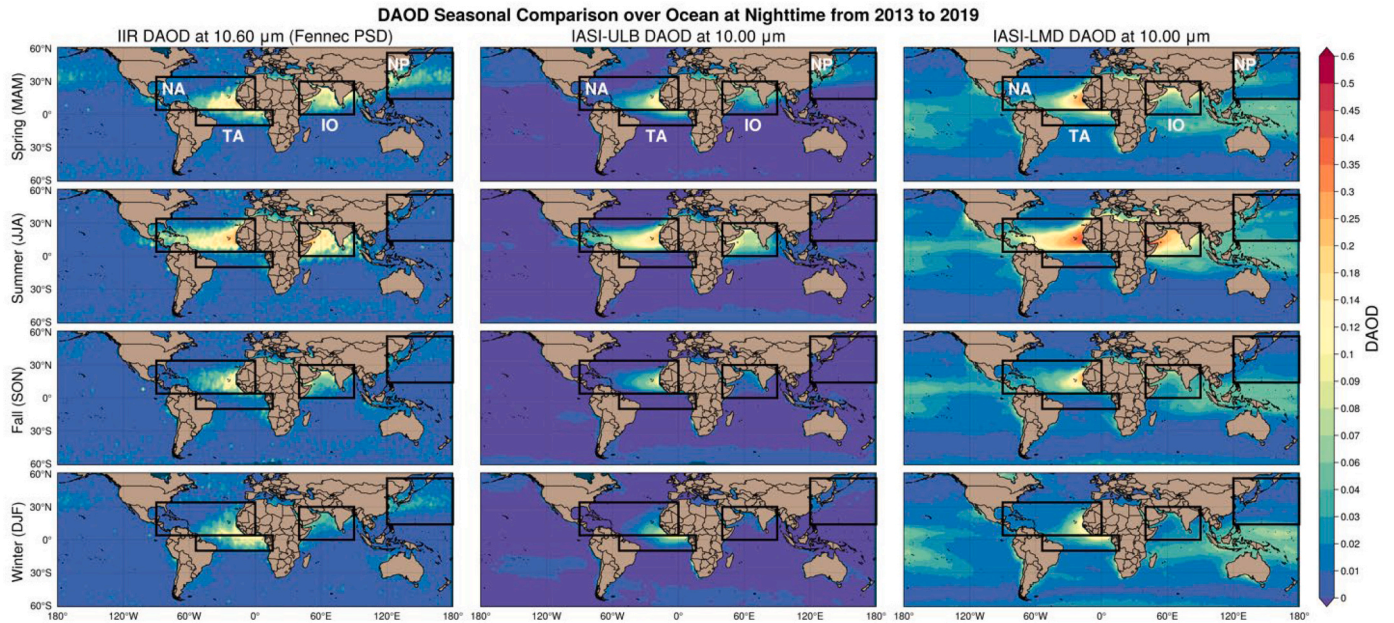


Fig. 15. The seasonal averaged global distribution of Fennec DAOD_{10.6 μm} (left columns), IASI-ULB DAOD_{10μm} (middle columns) and IASI-LMD DAOD_{10μm} (right columns). From up to down represents seasons from spring to winter. The black boxes represent the four active dust transport regions. The white texts within the top panels indicate the name of the four active dust transport regions. NA: North Atlantic; TA: Tropical Atlantic; IO: Indian Ocean; NP: North Pacific.

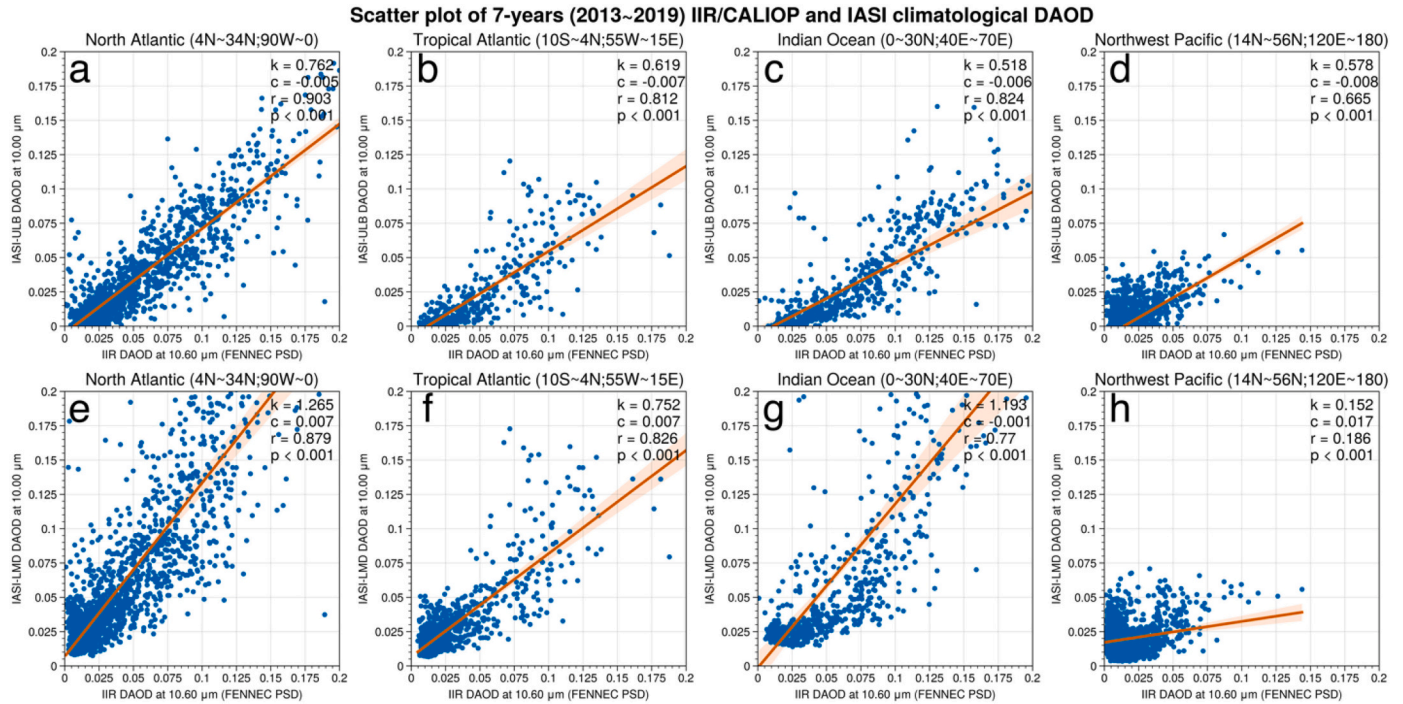


Fig. 16. The scatter plot of Fennec DAOD_{10.6 μm} versus IASI-ULB and IASI-LMD DAOD_{10μm} over NA (a,e), TA (b,f), IO (c,g) and NP (d,h). Red lines with orange shadow represent the linear regression and its standard error. The k , c , r and p at the upper right of each panel represent the slope, intercept, correlation coefficient and p -value of the linear regression. (For interpretation of the references to color in this figure legend, the reader is referred to the web version of this article.)

performance than that of IASI-only for dust transported from Asia.

In summary, despite the discrepancies over the low DAOD areas, the IIR-CALIO retrieval is well-agreed with two IASI retrievals on the seasonal variation of dust transport over NA, TA, and IO with confident correlations. In NP, the IIR-CALIO retrieval reveals a more apparent trend of dust transport than both IASI retrievals at around 30°N. Regarding DAOD value, which is deviated among the three retrievals, further comparison of DAOD_{10.6μm} with the well-trusted ground-based

AERONET measurement is necessary.

4.3. Seasonal and interannual comparison with AERONET coarse-mode AOD

Most DAOD_{TIR} retrieval studies estimate the results through the collocated comparison with the AERONET coarse-mode AOD in VIS (500 nm; refer to as “AOD_{500nm}”) at the dust-dominated sites (Capelle

et al., 2018; Capelle et al., 2014; Clarisse et al., 2019; Klüser et al., 2011; Peyridieu et al., 2013). However, the simultaneously collocated comparison of CALIPSO with AERONET needs to be within 40 km with a time window of ± 30 mins of the overpass time to have a rigorous comparison (Omar et al., 2013; Schuster et al., 2012). In addition, the quantitative comparison with AOD_{500nm} requires the TIR/VIS ratio. With the limited information of dust properties, the assumed TIR/VIS ratio could significantly error the comparison results (Capelle et al., 2018), even if the AOD_{500nm} from dust-dominated sites. Alternatively, in this section, we make the seasonal and interannual comparison of the collocated $1^\circ \times 1^\circ$ monthly mean grid-level DAOD_{10.6 μ m} with AOD_{500nm}. This approach aims to evaluate the consistency between DAOD_{10.6 μ m} and AOD_{500nm}, which has been used to evaluate CALIOP DAOD_{532nm} and AOD_{500nm} (Yu et al., 2015a). Without considering the TIR/VIS ratio, it is unnecessary to guarantee the AOD_{500nm} contributed purely by dust. Therefore, we select 97 AERONET sites within the defined dust-concentrated area (see Fig. 1a) over oceans from 2013 to 2019, as

shown in Fig. 17a. Meanwhile, as a reference, the two monthly mean IASI-retrieved DAOD_{10 μ m} are derived from the IASI-ULB and IASI-LMD level-2 products.

In Fig. 17b, the correlation coefficient between DAOD_{10.6 μ m} and AOD_{500nm} is 0.766, suggesting that the IIR-CALIOP retrieval agrees reasonably well with AERONET coarse-mode AOD on the seasonal and interannual variations. Note that the correlation coefficient of IASI-ULB DAOD_{10 μ m} with AOD_{500nm} and IASI-LMD DAOD_{10 μ m} with AOD_{500nm} are 0.932 and 0.861, respectively. Because of the higher sampling rate of IASI retrieval than IIR-CALIOP, the IASI-AERONET comparison pairs are 50% more than IIR-AERONET. As a result, we found better correlations in IASI-AERONET comparisons. In addition, the IIR-matched AOD_{500nm} is 17% higher and more fluctuated than IASI-matched AOD_{500nm}. Bearing the +17% difference in the number of pairs, we still found that the interannual mean DAOD_{10.6 μ m} is 64% larger than IASI-ULB DAOD_{10 μ m} and 52% less than that of DAOD_{10.6 μ m}. It implies that the IIR-CALIOP retrieved DAOD_{10.6 μ m} agrees better with IASI-ULB

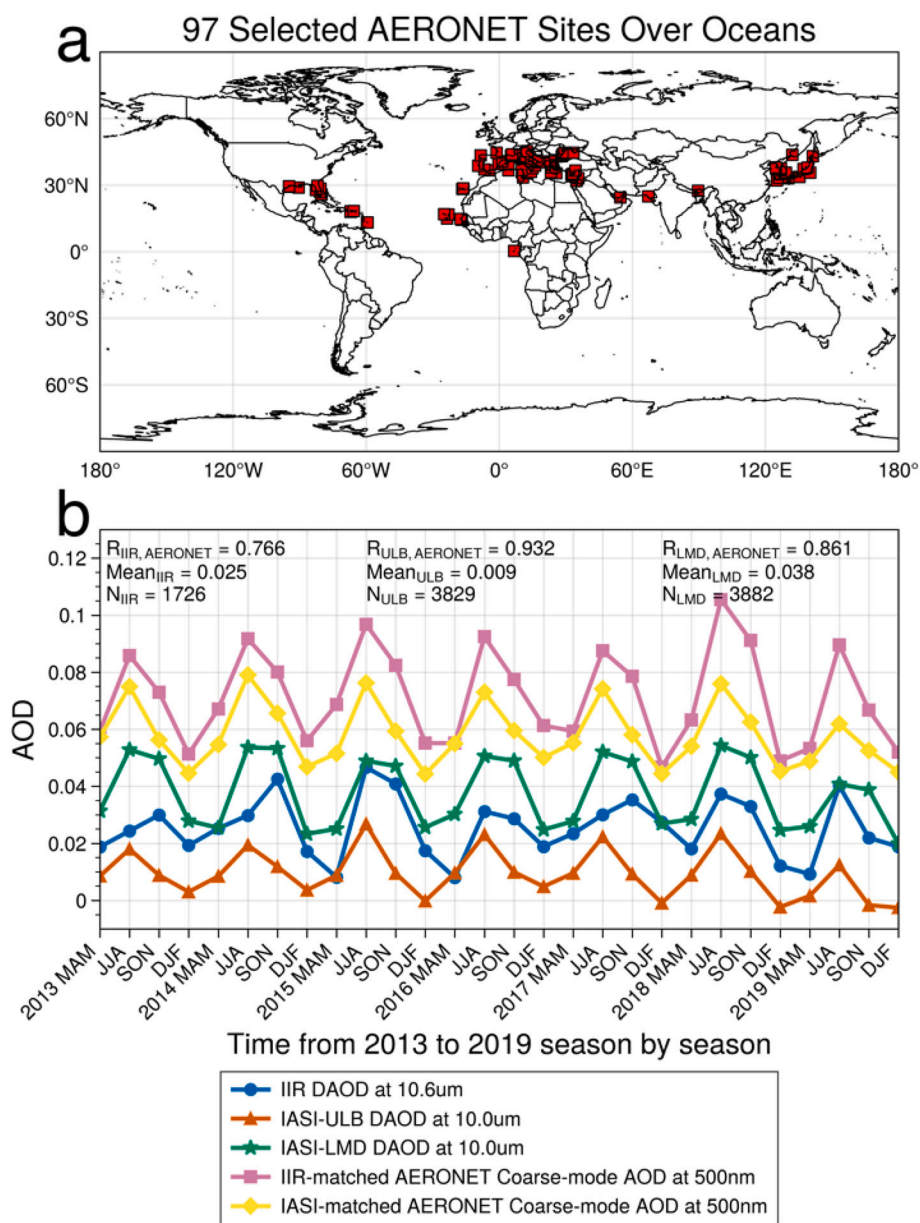


Fig. 17. (a) The geolocation of 97 selected AERONET sites. (b) The seasonal interannual variation of IIR-CALIOP DAOD_{10.6 μ m} (blue dot), IASI-ULB DAOD_{10 μ m} (red triangle), IASI-LMD DAOD_{10 μ m} (green star) and AERONET AOD_{500nm} paired with IIR-CALIOP (pink square) and IASI (yellow diamond) from 2013 to 2019. (For interpretation of the references to color in this figure legend, the reader is referred to the web version of this article.)

DAOD_{10μm}.

5. Summary and conclusions

This paper introduces a novel way to retrieve DAOD_{TIR} using the integrated CALIOP and IIR observations with a priori dust assumptions based on the state-of-art databases. The retrieval method is based on the BT contrast between the observed BT at the IIR 10.6 μm channel of the cloud-free dust scenario and the simulated cloud-free clean BT with corresponding assumed atmospheric and surface conditions. Thanks to the derived dust vertical distribution from CALIOP, the straightforward LUT depends on DAOD only, which can be built simultaneously with the cloud-free dust detection process. In addition, the 1-km resolution of IIR observation maximally reduces the sub-pixel cloud contamination on the dust radiative signal. Thus, we evaluated the retrieval uncertainties from the instrumental noise, ancillary data, radiative simulation and the a priori dust assumptions and produced climatological retrieval results (i.e., DAOD_{10.6μm}).

According to the non-spherical dust scattering properties calculation based on the spheroid shape distribution and the Di-Biagio RI database, the dust PSD assumption is the main contribution to the variation of TIR/VIS ratio in TIR atmospheric window bands, which would produce significantly different DAOD_{TIR} even with identical DAOD_{VIS}. However, with the TIR observation, the difference of retrieved DAOD_{TIR} caused by dust PSD assumptions is remarkably reduced. Combining with the synergic VIS observation offers an exciting prospect on constraining the DAOD_{TIR}, the dust particle size and further the DRE_{LW} uncertainty.

The comparison between DAOD_{10.6μm} and IASI-retrieved DAOD_{10μm} developed by the LMD and ULB groups is performed on a 7-year climatological scale with the assurance of sampling procedures. In general, DAOD_{10.6μm} shows good agreements of seasonal variations of dust transport with both IASI DAOD_{10μm} over the active dust transport regions but with deviations on the mean DAOD. Discrepancies over the low DAOD areas are possibly due to the difference in sampling approach (i.e., cloud masking and dust detection), retrieval methods and the 10.0 μm-to-10.6 μm spectral difference. Despite that, the consistency of the retrieved DAOD_{10.6μm} with AERONET observation is presented through the seasonal and interannual comparison with AERONET coarse-mode AOD over 97 selected sites over oceans.

The study presented here has several limitations. First of all, the limited spatial coverage of CALIOP and the nighttime-only retrieval leads to a relatively low DAOD_{TIR} sampling rate. Secondly, as the highly varied surface emissivity and skin temperature over land would have significant uncertainties, the retrieval is operated over oceans only. Thirdly, the single-band retrieval approach is subject to massive uncertainties from the atmospheric gas absorptions, the instrumental noise, and the radiative transfer simulation. Moreover, it has insufficient information content for retrieving other dust properties such as dust PSD and RI. The retrieval can be improved by adding more information from other channels/instruments and better a priori assumptions. Therefore, the future developments on the current retrieval method to address the remaining challenges are listed below:

- 1) Propagate the retrieval to the 60-km IIR swath by assuming the vertical distribution of dust from CALIOP within a reasonable scale.
- 2) Seeking more helpful information from other IIR channels and/or collocated instruments in the A-Train (e.g., MODIS and AIRS) for constraining the retrieval uncertainties, exploring more retrievable properties, and expanding the spatial coverage of the retrieval.

Data availability

The 2007 to 2020 IIR-CALIOP DAOD data (L2 and 1° × 1° monthly L3) presented in this study are available at Mendeley Data, DOI: 10.17632/bd85vzyf96.3). The data will be operationally updated with the IIR and CALIOP products and will be expanded when improvements

are performed in future studies.

Declaration of Competing Interest

Zhibo Zhang reports financial support was provided by NASA.

Acknowledgement

JZ, ZZ and AG are supported by a NASA grant (no. 80NSSC20K0130) from the CALIPSO and CloudSat program managed by David Considine. HY was supported by the CloudSat/CALIPSO program. The computations in this study were performed at the UMBC High Performance Computing Facility (HPCF). The facility is supported by the US National Science Foundation through the MRI program (grant nos. CNS-0821258 and CNS-1228778) and the SCREMS program (grant no. DMS-0821311), with substantial support from UMBC. We acknowledge the AERIS data infrastructure for providing access to the IASI-LMD data in this study and CNRS-LMD for the development of the retrieval algorithms. We thank the ICARE Data and Services Center for providing access to the IASI-ULB data in this study at <http://www.icare.univ-lille1.fr/>. We thank NASA for providing the IIR and CALIOP data, which are available at <https://asdc.larc.nasa.gov/data/CALIPSO/>. We also thank the AERONET project at NASA/GSFC for providing the ground-based aerosol data. Last but not least, we acknowledge and thank four anonymous reviewers who provide insightful comments and recommendations.

References

- Adebisi, A.A., Kok, J.F., 2020. Climate models miss most of the coarse dust in the atmosphere. *Sci. Adv.* 6 eaaz9507.
- Banerjee, P., Satheesh, S.K., Moorthy, K.K., Nanjundiah, R.S., Nair, V.S., 2019. Long-range transport of mineral dust to the Northeast Indian Ocean: regional versus remote sources and the implications. *J. Clim.* 32, 1525–1549.
- Capelle, V., Chédin, A., Siméon, M., Tsamalis, C., Pierangelo, C., Pondrom, M., Crevoisier, C., Crepeau, L., Scott, N.A., 2014. Evaluation of IASI-derived dust aerosol characteristics over the tropical belt. *Atmos. Chem. Phys.* 14.
- Capelle, V., Chédin, A., Pondrom, M., Crevoisier, C., Armante, R., Crepeau, L., Scott, N.A., 2018. Infrared dust aerosol optical depth retrieved daily from IASI and comparison with AERONET over the period 2007–2016. *Remote Sens. Environ.* 206, 15–32.
- Chen, B., Huang, J., Minnis, P., Hu, Y., Yi, Y., Liu, Z., Zhang, D., Wang, X., 2010. Detection of dust aerosol by combining CALIPSO active lidar and passive IIR measurements. *Atmos. Chem. Phys.* 10, 4241–4251.
- Chen, B., Zhang, P., Zhang, B., Jia, R., Zhang, Z., Wang, T., Zhou, T., 2014. An overview of passive and active dust detection methods using satellite measurements. *J. Meteorol. Res.* 28, 1029–1040.
- Chiappello, I., Moulin, C., 2002. TOMS and METEOSAT satellite records of the variability of Saharan dust transport over the Atlantic during the last two decades (1979–1997). *Geophys. Res. Lett.* 29, 17–11–17–14.
- Chooabari, O.A., Zawar-Reza, P., Sturman, A., 2014. The global distribution of mineral dust and its impacts on the climate system: a review. *Atmos. Res.* 138, 152–165.
- Christopher, S.A., Jones, T.A., 2010. Satellite and surface-based remote sensing of Saharan dust aerosols. *Remote Sens. Environ.* 114, 1002–1007.
- Clarisse, L., Clerbaux, C., Franco, B., Hadji-Lazaro, J., Whitburn, S., Kopp, A.K., Hurtmans, D., Coheur, P.-F., 2019. A decadal data set of global atmospheric dust retrieved from IASI satellite measurements. *J. Geophys. Res. Atmos.* 124, 1618–1647.
- Cuesta, J., Eremenko, M., Flamant, C., Dufour, G., Laurent, B., Bergametti, G., Höpfner, M., Orphal, J., Zhou, D., 2015. Three-dimensional distribution of a major desert dust outbreak over East Asia in March 2008 derived from IASI satellite observations. *J. Geophys. Res. Atmos.* 120, 7099–7127.
- DeSouza-Machado, S.G., Strow, L.L., Hannon, S.E., Motteler, H.E., 2006. Infrared dust spectral signatures from AIRS. *Geophys. Res. Lett.* 33.
- Di Biagio, C., Formenti, P., Balkanski, Y., Caponi, L., Cazaunau, M., Pangui, E., Journe, E., Nowak, S., Caquineau, S., Andreae, M.O., Kandler, K., Saeed, T., Piketh, S., Seibert, D., Williams, E., Doussin, J.-F., 2017. Global scale variability of the mineral dust longwave refractive index: a new dataset of in situ measurements for climate modeling and remote sensing. *Atmos. Chem. Phys.* 17, 1901–1929.
- Di Biagio, C., Balkanski, Y., Albani, S., Boucher, O., Formenti, P., 2020. Direct radiative effect by mineral dust aerosols constrained by new microphysical and spectral optical data. *Geophys. Res. Lett.* 47 e2019GL086186.
- Di Biagio, C., Banks, J.R., Gaetani, M., 2021. Dust atmospheric transport over long distances. In: *Reference Module in Earth Systems and Environmental Sciences*. Elsevier.
- Dubovik, O., Smirnov, A., Holben, B., King, M., Kaufman, Y., Eck, T., Slutsker, I., 2000. Accuracy assessments of aerosol optical properties retrieved from aerosol robotic

- network (AERONET) Sun and sky radiance measurements. *J. Geophys. Res. Atmos.* 105, 9791–9806.
- Dubovik, O., Holben, B., Eck, T.F., Smirnov, A., Kaufman, Y.J., King, M.D., Tanré, D., Slutsker, I., 2002. Variability of absorption and optical properties of key aerosol types observed in worldwide locations. *J. Atmos. Sci.* 59, 590–608.
- Dubovik, O., Sinyuk, A., Lapyonok, T., Holben, B.N., Mishchenko, M., Yang, P., Eck, T.F., Volten, H., Muñoz, O., Veihelmann, B., 2006. Application of spheroid models to account for aerosol particle nonsphericity in remote sensing of desert dust. *J. Geophys. Res. Atmos.* 111.
- Dubuisson, P., Giraud, V., Chomette, O., Chepfer, H., Pelon, J., 2005. Fast radiative transfer modeling for infrared imaging radiometry. *J. Quant. Spectrosc. Radiat. Transf.* 95, 201–220.
- Dubuisson, P., Giraud, V., Pelon, J., Cadet, B., Yang, P., 2008. Sensitivity of thermal infrared radiation at the top of the atmosphere and the surface to ice cloud microphysics. *J. Appl. Meteorol. Climatol.* 47, 2545–2560.
- Dunion, J.P., Velden, C.S., 2004. The impact of the Saharan air layer on Atlantic tropical cyclone activity. *Bull. Am. Meteorol. Soc.* 85, 353–366.
- Evan, A.T., Dunion, J., Foley, J.A., Heidinger, A.K., Velden, C.S., 2006. New evidence for a relationship between Atlantic tropical cyclone activity and African dust outbreaks. *Geophys. Res. Lett.* 33.
- Gama, C., Tchepel, O., Baldasano, J.M., Basart, S., Ferreira, J., Pio, C., Cardoso, J., Borrego, C., 2015. Seasonal patterns of Saharan dust over Cape Verde – a combined approach using observations and modelling. *Tellus Ser. B Chem. Phys. Meteorol.* 67, 24410.
- Garnier, A., Pelon, J., Dubuisson, P., Faivre, M., Chomette, O., Pascal, N., Kratz, D.P., 2012. Retrieval of cloud properties using CALIPSO imaging infrared radiometer. Part I: effective emissivity and optical depth. *J. Appl. Meteorol. Climatol.* 51, 1407–1425.
- Garnier, A., Scott, N.A., Pelon, J., Armante, R., Crépeau, L., Six, B., Pascal, N., 2017. Long-term assessment of the CALIPSO imaging infrared radiometer (IIR) calibration and stability through simulated and observed comparisons with MODIS/Aqua and SEVIRI/Meteosat. *Atmos. Meas. Tech.* 10, 1403–1424.
- Garnier, A., Trémas, T., Pelon, J., Lee, K.-P., Nobileau, D., Gross-Colzy, L., Pascal, N., Ferrage, P., Scott, N.A., 2018. CALIPSO IIR version 2 level 1b calibrated radiances: analysis and reduction of residual biases in the northern hemisphere. *Atmos. Meas. Tech.* 11, 2485–2500.
- Garnier, A., Pelon, J., Pascal, N., Vaughan, M.A., Dubuisson, P., Yang, P., Mitchell, D.L., 2021. Version 4 CALIPSO imaging infrared radiometer ice and liquid water cloud microphysical properties – part I: the retrieval algorithms. *Atmos. Meas. Tech.* 14, 3253–3276.
- Gelaro, R., McCarty, W., Suárez, M.J., Todling, R., Molod, A., Takacs, L., Randles, C.A., Darmenov, A., Bosilovich, M.G., Reichle, R., Wargan, K., Coy, L., Cullather, R., Draper, C., Akella, S., Buchard, V., Conaty, A., da Silva, A.M., Gu, W., Kim, G.-K., Koster, R., Lucchesi, R., Merkova, D., Nielsen, J.E., Partyka, G., Pawson, S., Putman, W., Rienecker, M., Schubert, S.D., Sienkiewicz, M., Zhao, B., 2017. The modern-era retrospective analysis for research and applications, version 2 (MERRA-2). *J. Clim.* 30, 5419–5454.
- Gkikas, A., Obiso, V., Pérez García-Pando, C., Jorba, O., Hatzianastassiou, N., Vendrell, L., Basart, S., Solomos, S., Gassó, S., Baldasano, J.M., 2018. Direct radiative effects during intense Mediterranean desert dust outbreaks. *Atmos. Chem. Phys.* 18, 8757–8787.
- Goudie, A.S., Middleton, N.J., 2006. *Desert Dust in the Global System*. Springer Science & Business Media.
- Griffin, D.W., 2007. Atmospheric movement of microorganisms in clouds of desert dust and implications for human health. *Clin. Microbiol. Rev.* 20, 459–477.
- Gupta, G., Ratnam, M.V., Madhavan, B.L., Prasad, P., Narayanamurthy, C.S., 2021. Vertical and spatial distribution of elevated aerosol layers obtained using long-term ground-based and space-borne lidar observations. *Atmos. Environ.* 246, 118172.
- Gutleben, M., Groß, S., Wirth, M., Emde, C., Mayer, B., 2019. Impacts of water vapor on Saharan air layer radiative heating. *Geophys. Res. Lett.* 46, 14854–14862.
- Hess, M., Koepke, P., Schult, I., 1998. Optical properties of aerosols and clouds: the software package OPAC. *Bull. Am. Meteorol. Soc.* 79, 831–844.
- Huang, J., Minnis, P., Chen, B., Huang, Z., Liu, Z., Zhao, Q., Yi, Y., Ayers, J.K., 2008. Long-range transport and vertical structure of Asian dust from CALIPSO and surface measurements during PACDEX. *J. Geophys. Res. Atmos.* 113, 113. <https://doi.org/10.1029/2008jd010620>.
- Kaplan, C., 2013. An Investigation of Sub-Pixel Cloud/Clear-Sky Contamination Using Hyper-Spectral AVIRIS Data.
- Kim, M.-H., Omar, A.H., Tackett, J.L., Vaughan, M.A., Winker, D.M., Trepte, C.R., Hu, Y., Liu, Z., Poole, L.R., Pitts, M.C., 2018. The CALIPSO version 4 automated aerosol classification and lidar ratio selection algorithm. *Atmos. Meas. Tech.* 11, 6107.
- Klüser, L., Martynenko, D., Holzer-Popp, T., 2011. Thermal infrared remote sensing of mineral dust over land and ocean: a spectral SVD based retrieval approach for IASI. *Atmos. Meas. Tech.* 4, 757–773.
- Klüser, L., Kleiber, P., Holzer-Popp, T., Grassian, V.H., 2012. Desert dust observation from space – application of measured mineral component infrared extinction spectra. *Atmos. Environ.* 54, 419–427.
- Klüser, L., Banks, J.R., Martynenko, D., Bergemann, C., Brindley, H.E., Holzer-Popp, T., 2015. Information content of space-borne hyperspectral infrared observations with respect to mineral dust properties. *Remote Sens. Environ.* 156, 294–309.
- Kok, J.F., Ridley, D.A., Zhou, Q., Miller, R.L., Zhao, C., Heald, C.L., Ward, D.S., Albani, S., Haustein, K., 2017. Smaller desert dust cooling effect estimated from analysis of dust size and abundance. *Nat. Geosci.* 10, 274–278.
- Lee, K.H., Wong, M.S., Chung, S.-R., Sohn, E., 2014. Improved volcanic ash detection based on a hybrid reverse absorption technique. *Atmos. Res.* 143, 31–42.
- Li, Z., Wang, Y., Guo, J., Zhao, C., Cribb, M.C., Dong, X., Fan, J., Gong, D., Huang, J., Jiang, M., Jiang, Y., Lee, S.-S., Li, H., Li, J., Liu, J., Qian, Y., Rosenfeld, D., Shan, S., Sun, Y., Wang, H., Xin, J., Yan, X., Yang, X., Yang, X.-q., Zhang, F., Zheng, Y., 2019. East Asian study of tropospheric aerosols and their impact on regional clouds, precipitation, and climate (EAST-AIRPCP). *J. Geophys. Res. Atmos.* 124, 13026–13054.
- Liu, Z., Omar, A., Vaughan, M., Hair, J., Kittaka, C., Hu, Y., Powell, K., Trepte, C., Winker, D., Hostetler, C., Ferrare, R., Pierce, R., 2008. CALIPSO lidar observations of the optical properties of Saharan dust: a case study of long-range transport. *J. Geophys. Res. Atmos.* 113.
- Liu, Z., Vaughan, M., Winker, D., Kittaka, C., Getzewich, B., Kuehn, R., Omar, A., Powell, K., Trepte, C., Hostetler, C., 2009. The CALIPSO lidar cloud and aerosol discrimination: version 2 algorithm and initial assessment of performance. *J. Atmos. Ocean. Technol.* 26, 1198–1213.
- Liu, Z., Kuehn, R., Vaughan, M., Winker, D., Omar, A., Powell, K., Trepte, C., Hu, Y., Hostetler, C., 2010. The CALIPSO cloud and aerosol discrimination: version 3 algorithm and test results. In: 25th International Laser Radar Conference (ILRC), St. Petersburg, Russia, pp. 5–9.
- Liu, Z., Kar, J., Zeng, S., Tackett, J., Vaughan, M., Avery, M., Pelon, J., Getzewich, B., Lee, K.-P., Magill, B., 2019. Discriminating between Clouds and Aerosols in the CALIOP Version 4.1 Data Products.
- Mahowald, N., Albani, S., Kok, J.F., Engelstaedter, S., Scanza, R., Ward, D.S., Flanner, M. G., 2014. The size distribution of desert dust aerosols and its impact on the earth system. *Aeolian Res.* 15, 53–71.
- Maring, H., Savoie, D.L., Izaguirre, M.A., Custals, L., Reid, J.S., 2003. Mineral dust aerosol size distribution change during atmospheric transport. *J. Geophys. Res. Atmos.* 108.
- Martins, J.V., Tanré, D., Remer, L., Kaufman, Y., Mattoo, S., Levy, R., 2002. MODIS cloud screening for remote sensing of aerosols over oceans using spatial variability. *Geophys. Res. Lett.* 29, MOD4-1-MOD4-4.
- Mishchenko, M.I., 2000. Calculation of the amplitude matrix for a non-spherical particle in a fixed orientation. *Appl. Opt.* 39, 1026–1031.
- Mishchenko, M.I., Travis, L.D., Kahn, R.A., West, R.A., 1997. Modeling phase functions for dustlike tropospheric aerosols using a shape mixture of randomly oriented polydisperse spheroids. *J. Geophys. Res. Atmos.* 102, 16831–16847.
- Omar, A.H., Winker, D.M., Tackett, J.L., Giles, D.M., Kar, J., Liu, Z., Vaughan, M.A., Powell, K.A., Trepte, C.R., 2013. CALIOP and AERONET aerosol optical depth comparisons: one size fits none. *J. Geophys. Res. Atmos.* 118, 4748–4766.
- Peyridieu, S., Chédin, A., Tanré, D., Capelle, V., Pierangelo, C., Lamquin, N., Armante, R., 2010. Saharan dust infrared optical depth and altitude retrieved from AIRS: a focus over North Atlantic & comparison to MODIS and CALIPSO. *Atmos. Chem. Phys.* 10, 1953–1967.
- Peyridieu, S., Chédin, A., Capelle, V., Tsalamis, C., Pierangelo, C., Armante, R., Crevoisier, C., Crépeau, L., Siméon, M., Ducos, F., Scott, N.A., 2013. Characterisation of dust aerosols in the infrared from IASI and comparison with PARASOL, MODIS, MISR, CALIOP, and AERONET observations. *Atmos. Chem. Phys.* 13, 6065–6082.
- Pierangelo, C., Chédin, A., Heilliet, S., Jacquinet-Husson, N., Armante, R., 2004. Dust altitude and infrared optical depth from AIRS. *Atmos. Chem. Phys.* 4, 1813–1822.
- Pierangelo, C., Chédin, A., Legrand, M., 2013. Longwave passive remote sensing. In: Lenoble, J., Remer, L., Tanré, D. (Eds.), *Aerosol Remote Sensing*. Springer Berlin Heidelberg, Berlin, Heidelberg, pp. 223–281.
- Querol, X., Tobias, A., Pérez, N., Karanasiou, A., Amato, F., Stafoggia, M., Pérez García-Pando, C., Ginoux, P., Forastiere, F., Gumy, S., Mudu, P., Alastuey, A., 2019. Monitoring the impact of desert dust outbreaks for air quality for health studies. *Environ. Int.* 130, 104867.
- Read, W.G., Froidevaux, L., Waters, J.W., 1993. Microwave limb sounder measurement of stratospheric SO₂ from the Mt. Pinatubo Volcano. *Geophys. Res. Lett.* 20, 1299–1302.
- Ryder, C.L., Highwood, E.J., Lai, T.M., Sodemann, H., Marsham, J.H., 2013a. Impact of atmospheric transport on the evolution of microphysical and optical properties of Saharan dust. *Geophys. Res. Lett.* 40, 2433–2438.
- Ryder, C.L., Highwood, E.J., Rosenberg, P.D., Trembath, J., Brooke, J.K., Bart, M., Dean, A., Crosier, J., Dorsey, J., Brindley, H., Banks, J., Marsham, J.H., McQuaid, J. B., Sodemann, H., Washington, R., 2013b. Optical properties of Saharan dust aerosol and contribution from the coarse mode as measured during the Fennec 2011 aircraft campaign. *Atmos. Chem. Phys.* 13, 303–325.
- Ryder, C.L., Highwood, E.J., Walser, A., Seibert, P., Philipp, A., Weinzierl, B., 2019. Coarse and giant particles are ubiquitous in Saharan dust export regions and are radiatively significant over the Sahara. *Atmos. Chem. Phys.* 19, 15353–15376.
- Satheesh, S.K., Moorthy, K.K., 2005. Radiative effects of natural aerosols: a review. *Atmos. Environ.* 39, 2089–2110.
- Sayer, A.M., Smirnov, A., Hsu, N.C., Holben, B.N., 2012. A pure marine aerosol model, for use in remote sensing applications. *J. Geophys. Res. Atmos.* 117.
- Schuster, G.L., Vaughan, M., MacDonnell, D., Su, W., Winker, D., Dubovik, O., Lapyonok, T., Trepte, C., 2012. Comparison of CALIPSO aerosol optical depth retrievals to AERONET measurements, and a climatology for the lidar ratio of dust. *Atmos. Chem. Phys.* 12, 7431–7452.
- Sokolik, I.N., Toon, O.B., Bergstrom, R.W., 1998. Modeling the radiative characteristics of airborne mineral aerosols at infrared wavelengths. *J. Geophys. Res. Atmos.* 103, 8813–8826.
- Song, Q., Zhang, Z., Yu, H., Kato, S., Yang, P., Colarco, P., Remer, L.A., Ryder, C.L., 2018. Net radiative effects of dust in the tropical North Atlantic based on integrated satellite observations and in situ measurements. *Atmos. Chem. Phys.* 18, 11303–11322.
- Song, Q., Zhang, Z., Yu, H., Ginoux, P., Shen, J., 2021. Global dust optical depth climatology derived from CALIOP and MODIS aerosol retrievals on decadal timescales: regional and interannual variability. *Atmos. Chem. Phys.* 21, 13369–13395.

- Stamnes, K., Tsay, S.C., Wiscombe, W., Jayaweera, K., 1988. Numerically stable algorithm for discrete-ordinate-method radiative transfer in multiple scattering and emitting layered media. *Appl. Opt.* 27, 2502–2509.
- Taylor, I., Mackie, S., Watson, M., 2015. Investigating the use of the Saharan dust index as a tool for the detection of volcanic ash in SEVIRI imagery. *J. Volcanol. Geotherm. Res.* 304, 126–141.
- Tegen, I., Lacis, A.A., 1996. Modeling of particle size distribution and its influence on the radiative properties of mineral dust aerosol. *J. Geophys. Res. Atmos.* 101, 19237–19244.
- Tegen, I., Lacis, A.A., Fung, I., 1996. The influence on climate forcing of mineral aerosols from disturbed soils. *Nature* 380, 419–422.
- Thorsen, T.J., Ferrare, R.A., Kato, S., Winker, D.M., 2020. Aerosol direct radiative effect sensitivity analysis. *J. Clim.* 33, 6119–6139.
- Torres, O., Bhartia, P., Herman, J., Ahmad, Z., Gleason, J., 1998. Derivation of aerosol properties from satellite measurements of backscattered ultraviolet radiation: theoretical basis. *J. Geophys. Res. Atmos.* 103, 17099–17110.
- Vaughan, M.A., Winker, D.M., Powell, K.A., 2005. CALIOP algorithm theoretical basis document, part 2: feature detection and layer properties algorithms. Rep. PC-SCI 202, 87.
- Volz, F.E., 1973. Infrared optical constants of ammonium sulfate, sahara dust, volcanic pumice, and flyash. *Appl. Opt.* 12, 564–568.
- Wang, W., Huang, J., Minnis, P., Hu, Y., Li, J., Huang, Z., Ayers, J.K., Wang, T., 2010. Dusty cloud properties and radiative forcing over dust source and downwind regions derived from A-train data during the Pacific dust experiment. *J. Geophys. Res. Atmos.* 115.
- Winker, D.M., Tackett, J.L., Getzewich, B.J., Liu, Z., Vaughan, M.A., Rogers, R.R., 2013. The global 3-D distribution of tropospheric aerosols as characterized by CALIOP. *Atmos. Chem. Phys.* 13, 3345–3361.
- Wong, S., Dessler, A.E., Mahowald, N.M., Yang, P., Feng, Q., 2009. Maintenance of lower tropospheric temperature inversion in the Saharan air layer by dust and dry anomaly. *J. Clim.* 22, 5149–5162.
- Wu, M., Liu, X., Yu, H., Wang, H., Shi, Y., Yang, K., Darmanov, A., Wu, C., Wang, Z., Luo, T., Feng, Y., Ke, Z., 2020. Understanding processes that control dust spatial distributions with global climate models and satellite observations. *Atmos. Chem. Phys.* 20, 13835–13855.
- Xia, X.-a., Chen, H.-b., Wang, P.-c., 2004. Validation of MODIS aerosol retrievals and evaluation of potential cloud contamination in East Asia. *J. Environ. Sci.* 16, 832–837.
- Xu, C., Ma, Y., Yang, K., You, C., 2018. Tibetan plateau impacts global dust transport in the upper troposphere. *J. Clim.* 31, 4745–4756.
- Yang, W., Marshak, A., Várnai, T., Kalashnikova, O.V., Kostinski, A.B., 2012. CALIPSO observations of transatlantic dust: vertical stratification and effect of clouds. *Atmos. Chem. Phys.* 12, 11339–11354.
- Young, S.A., Vaughan, M.A., Kuehn, R.E., Winker, D.M., 2013. The retrieval of profiles of particulate extinction from Cloud–Aerosol Lidar and Infrared Pathfinder Satellite Observations (CALIPSO) data: uncertainty and error sensitivity analyses. *J. Atmos. Ocean. Technol.* 30, 395–428.
- Young, S.A., Vaughan, M.A., Garnier, A., Tackett, J.L., Lambeth, J.D., Powell, K.A., 2018. Extinction and optical depth retrievals for CALIPSO's version 4 data release. *Atmos. Meas. Tech.* 11.
- Yu, H., Kaufman, Y.J., Chin, M., Feingold, G., Remer, L.A., Anderson, T.L., Balkanski, Y., Bellouin, N., Boucher, O., Christopher, S., DeCola, P., Kahn, R., Koch, D., Loeb, N., Reddy, M.S., Schulz, M., Takemura, T., Zhou, M., 2006. A review of measurement-based assessments of the aerosol direct radiative effect and forcing. *Atmos. Chem. Phys.* 6, 613–666.
- Yu, H., Remer, L.A., Chin, M., Bian, H., Kleidman, R.G., Diehl, T., 2008. A satellite-based assessment of transpacific transport of pollution aerosol. *J. Geophys. Res.* 113, D14S12. <https://doi.org/10.1029/2007JD009349>.
- Yu, H., Chin, M., Winker, D.M., Omar, A.H., Liu, Z., Kittaka, C., Diehl, T., 2010. Global view of aerosol vertical distributions from CALIPSO lidar measurements and GOCART simulations: regional and seasonal variations. *J. Geophys. Res. Atmos.* 115.
- Yu, H., Remer, L.A., Chin, M., Bian, H., Tan, Q., Yuan, T., Zhang, Y., 2012. Aerosols from overseas rival domestic emissions over North America. *Science* 337, 566–569.
- Yu, H., Remer, L.A., Kahn, R.A., Chin, M., Zhang, Y., 2013. Satellite perspective of aerosol intercontinental transport: from qualitative tracking to quantitative characterization. *Atmos. Res.* 124, 73–100.
- Yu, H., Chin, M., Bian, H., Yuan, T., Prospero, J.M., Omar, A.H., Remer, L.A., Winker, D.M., Yang, Y., Zhang, Y., Zhang, Z., 2015a. Quantification of trans-Atlantic dust transport from seven-year (2007–2013) record of CALIPSO lidar measurements. *Remote Sens. Environ.* 159, 232–249.
- Yu, H., Chin, M., Yuan, T., Bian, H., Remer, L.A., Prospero, J.M., Omar, A., Winker, D., Yang, Y., Zhang, Y., 2015b. The fertilizing role of African dust in the Amazon rainforest: a first multiyear assessment based on data from cloud-aerosol Lidar and infrared pathfinder satellite observations. *Geophys. Res. Lett.* 42, 1984–1991.
- Yu, H., Tan, Q., Chin, M., Remer, L.A., Kahn, R.A., Bian, H., Kim, D., Zhang, Z., Yuan, T., Omar, A.H., Winker, D.M., Levy, R.C., Kalashnikova, O., Crepeau, L., Capelle, V., Chédin, A., 2019. Estimates of African dust deposition along the trans-Atlantic transit using the decadelong record of aerosol measurements from CALIOP, MODIS, MISR, and IASI. *J. Geophys. Res. Atmos.* 124, 7975–7996.
- Yu, H., Yang, Y., Wang, H., Tan, Q., Chin, M., Levy, R.C., Remer, L.A., Smith, S.J., Yuan, T., Shi, Y., 2020. Interannual variability and trends of combustion aerosol and dust in major continental outflows revealed by MODIS retrievals and CAM5 simulations during 2003–2017. *Atmos. Chem. Phys.* 20, 139–161.
- Zhou, D.K., Larar, A.M., Liu, X., 2013. MetOp-A/IASI observed continental thermal IR emissivity variations. *IEEE J. Sel. Top. Appl. Earth Obs. Remote Sens.* 6, 1156–1162.